

# Intrusion Induced Global Warming Preceding Continental Flood Basalt Volcanism

Xiaochuan Tian (✉ [xtian@ldeo.columbia.edu](mailto:xtian@ldeo.columbia.edu))

Lamont-Doherty Earth Observatory <https://orcid.org/0000-0003-0289-1794>

W Buck

Lamont-Doherty Earth Observatory

---

## Physical Sciences - Article

**Keywords:** tectonics, climate, paleoclimatology, global warming

**Posted Date:** May 11th, 2021

**DOI:** <https://doi.org/10.21203/rs.3.rs-73857/v1>

**License:** © ⓘ This work is licensed under a Creative Commons Attribution 4.0 International License.

[Read Full License](#)

---

1 **Title: Intrusions Induce Global Warming Prior to Continental Flood Basalt**  
2 **Volcanism**

3 **Authors:** Xiaochuan Tian and W. Roger Buck

4 **Affiliation:**

5 Lamont-Doherty Earth Observatory, Columbia University, Palisades, NY, USA.  
6

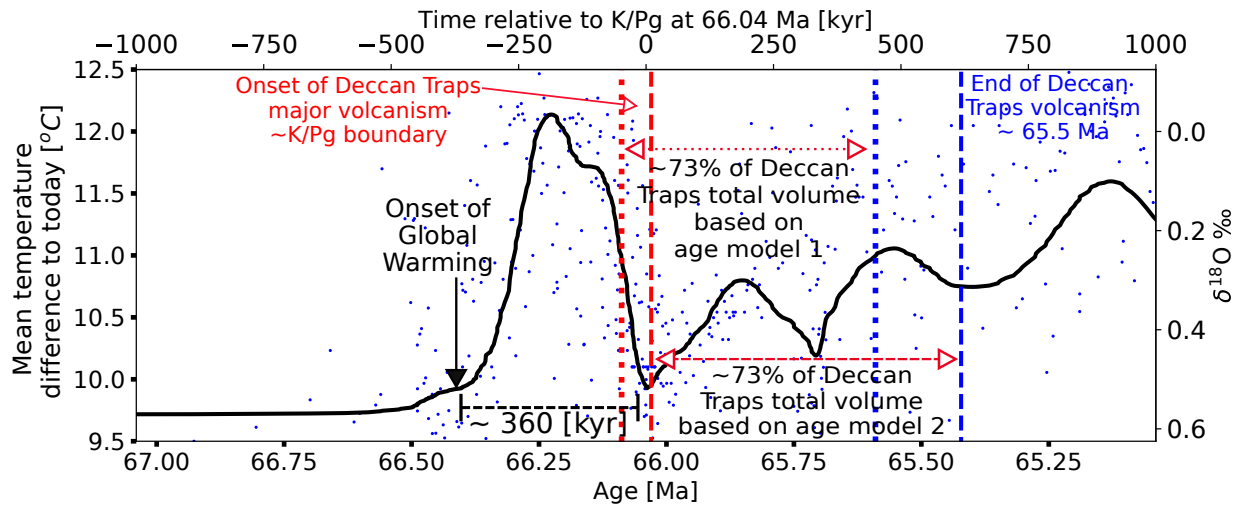
7 **Temporal correlations between continental flood basalt eruptions and mass extinctions**  
8 **have long been recognized<sup>1</sup>. Massive carbon degassing of Large Igneous Provinces can**  
9 **cause catastrophic global climatic and biotic perturbations<sup>1-3</sup>. However, recent high-**  
10 **precision geochronology from the Deccan Traps<sup>4,5</sup> and the Columbia River Basalt Group<sup>6</sup>**  
11 **challenges this causal link by showing that the major phase of flood basalts eruptions**  
12 **happened after the onset of global warming<sup>7-9</sup> by several hundred thousand years. Here,**  
13 **we argue that major eruptions of continental flood basalts may require densification of the**  
14 **crust by intrusion of larger volumes of magma than are extruded. Simple models show**  
15 **that magma crystallization and release of CO<sub>2</sub> from such intrusions could produce global**  
16 **warming before the main phase of flood basalt eruptions on the observed timescale. Our**  
17 **model, consistent with geological, geophysical, geochemical and paleoclimate data, suggests**  
18 **that the evolving crustal density has a first-order control on timing of the major phase of**  
19 **continental flood basalt volcanism. Degassing of CO<sub>2</sub> from LIP-related intrusions**  
20 **significantly affects Earth's climate and habitability.**

## 21 Introduction

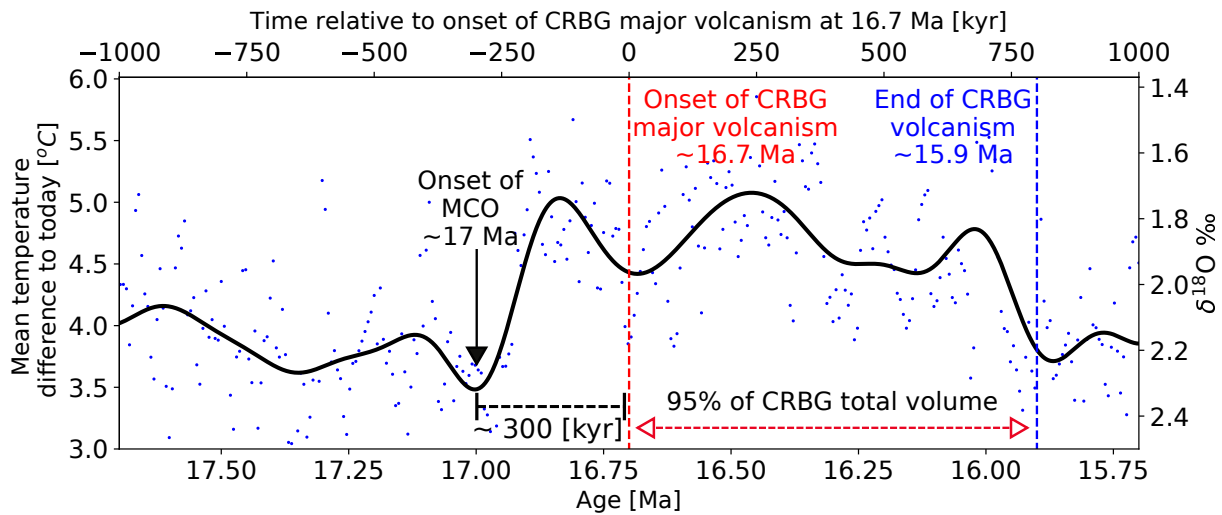
22 By far Earth's largest volcanic eruptions occur during the formation of continental  
23 flood basalts that define the surface extent of Large Igneous Provinces (LIPs). Major LIPs  
24 typically extrude more than  $10^6$  km<sup>3</sup> of magma within 1 million years <sup>2</sup>. Estimates of carbon  
25 dioxide (CO<sub>2</sub>) concentrations in primitive LIP magma vary from 0.1 to ~2 weight percent <sup>10</sup>, so  
26 that extrusions of a LIP could release as much as  $6 \times 10^{16}$  Kg of CO<sub>2</sub>. Such fluxes are enough to  
27 significantly warm Earth's climate <sup>7</sup>. The emplacement of LIPs are widely recognized to be  
28 coeval with climate changes and mass extinctions events <sup>1</sup>. These temporal correlations support  
29 the idea that flood basalt eruptions releasing massive amounts of greenhouse gases may cause  
30 climatic excursions and biotic crises.

31 Recent studies indicate that for at least two LIPs global warming began several hundred  
32 thousand years before the onset of the bulk of volcanism. For the Deccan traps, one of the largest  
33 LIPs, new data suggests that 73% of the flood basalts <sup>4,5,11</sup> were emplaced ~360 kyr after the  
34 onset of an average 2 °C global warming and before the Cretaceous-Paleogene (K/Pg) boundary <sup>7</sup>  
35 (Fig. 1a). For the Columbia River Basalt Group (CRBG), volcanic CO<sub>2</sub> release is a possible  
36 cause of the global warming and ice sheet melting during the Miocene Climate Optimum (MCO;  
37 17-14.7 Ma) <sup>12</sup>. However, recent basalt chronology data <sup>6</sup> indicates that 95% of the CRBG was  
38 erupted after 16.7 Ma, ~300 kyr after the onset of MCO <sup>8,9</sup> (Fig. 1b). The new data for both the  
39 Deccan Traps and the CRBG undermines the hypothetical causal link between LIP volcanism  
40 and global warming.

a Deccan Traps and K/Pg Global Warming



b Columbia River Basalt Group (CRBG) and Miocene Climate Optimum (MCO)



41

42 **Fig 1. Global temperature variations within 1000 kyr of the approximate onset of the main volcanic phases of**  
 43 **the Deccan Traps<sup>4,5</sup> and Columbia River Basalt Group<sup>6</sup> LIPs.** Black lines result from low-pass filtering of the  
 44 blue dots  $\delta^{18}O$  data and estimated temperature variations with time<sup>7-9</sup>. The age of onset and ending of the main  
 45 Deccan volcanic phase for two basalt dating methods are indicated by the pairs of vertical dashed lines. Vertical  
 46 arrows indicate that the onset of global warming for each case precedes the main volcanic phase by ~300 kyr.  
 47 Details of the age models and temperature estimates are described in the supplement.

48 Volcanoes are pathways for magma to reach Earth's surface, but for many volcanoes  
 49 more magma is intruded than is erupted<sup>13-15</sup>. For continental LIPs, geophysical data indicates  
 50 that from 3 to 16 times more magma is intruded as is extruded<sup>2,16,17</sup>. For example, below the

51 Deccan Traps and the CRBG higher-than-normal seismic velocities may indicate voluminous  
52 mafic crustal intrusions<sup>18-20</sup>. Geochemical studies of the CRBG also indicate up to 85% of total  
53 magma volume was emplaced within the crust<sup>21</sup>.

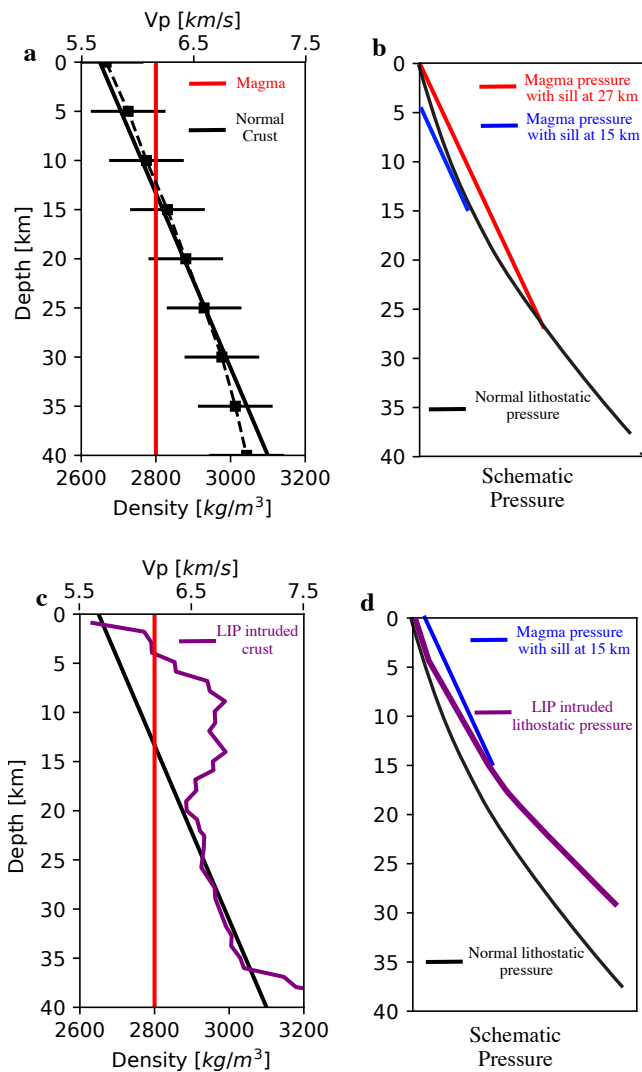
54 Crystallization releases nearly all carbon dioxide dissolved in basaltic magma<sup>22,23</sup>. Gas  
55 released from solidifying intruded magma should traverse the overlying crust through fractures,  
56 faults and hydrothermal vents<sup>24</sup>, as inferred for Yellowstone<sup>25</sup> or the East African Rift<sup>26</sup>. Thus,  
57 the intrusion and solidification of millions of cubic kilometers of basaltic LIP magma would  
58 release far more CO<sub>2</sub> than released by extrusion. If the intrusion precedes extrusion it would  
59 explain the pattern of global warming preceding LIP surface flows.

60 Geochemical studies indicate that mantle-derived magma resides for thousands of years  
61 in transcrustal magmatic systems before it extrudes<sup>27</sup>. For extrusion, the pressure in such magma  
62 reservoirs must be greater than the hydrostatic pressure at the base of a column of magma from  
63 the surface to the reservoirs. The long-term average pressure in a magma reservoir should equal  
64 the lithostatic pressure (the average density of the overlying crust times the acceleration of  
65 gravity and the depth below the surface). Magma reservoirs can be ‘overpressured’ relative to  
66 lithostatic pressure, but it is difficult to maintain overpressure if magma reservoirs are large  
67 and/or are surrounded by low viscosity crust<sup>28,29</sup>. For many LIPs crustal intrusions are thought  
68 to be very large, with lateral dimensions up to ~10<sup>3</sup> kilometers<sup>17,20,30</sup> so that overpressures  
69 should be negligible. Thus, large flood basalt extrusions may only happen when the average  
70 overburden density is greater than the magma density.

71 Particularly clear evidence for the importance of crustal density in controlling eruptions  
72 comes from plate spreading centers. Constraints on the depth of axial magma chambers (AMCs)  
73 and the crustal density structure at oceanic spreading centers are superior to those for continental

74 magma bodies due to the greater resolving power of marine seismic methods. AMCs are fairly  
75 small (~1 km wide) and are seen to lie at or below the depth where the average overburden  
76 density equals magma density, a depth that is termed the 'level of eruptibility' <sup>31,32</sup>.

77 Continental crustal density generally increases with depth and so the average density of  
78 overburden also increases with depth. Figure 2a shows the average seismic compressional wave  
79 velocities in continental crust with depth based on global seismic experiments <sup>33</sup>. Assuming a  
80 standard relation between seismic velocity and density for crustal rocks at different depths <sup>33</sup>, we  
81 infer the average crustal density structure based on the seismic velocities. Upper continental  
82 crust is composed of felsic rocks rich in low density minerals like quartz and feldspar while the  
83 lowermost crust is less felsic and so denser. Assuming a typical basaltic magma density of 2800  
84 kg m<sup>-3</sup> and a crustal density structure shown in Fig. 2a there should be enough pressure for  
85 eruptions only if the magma is sourced from reservoirs like sills that are deeper than the level of  
86 eruptibility at 27 km (Fig. 2b red). For sills at shallower depths (Fig. 2b blue) the magma should  
87 not reach the surface even with an open conduit to the surface.



88

89 **Fig. 2 | Illustrations of relations between seismic velocities, densities and pressures in typical continental crust**

90 **(a,b) and the crust under part of the Deccan LIP (c,d). a,** shows average continental P-wave velocity (dashed)

91 from ref<sup>33</sup> with density assuming a linear relation between velocity and density. Solid lines show densities assumed

92 in the model. Magma density is from ref.<sup>34</sup> **b,** black line shows lithostatic pressure for the density structure given

93 by solid line in a. Red line shows static pressure in a column of magma just reaching the surface while blue shows

94 the same for a column of magma with lithostatic pressure at 15 km depth. **c,** P-wave velocity and density profiles

95 beneath Deccan Traps are converted from refs.<sup>18,19</sup> using a Vs to Vp relationship (ref.<sup>35</sup>). **d,** Purple line shows

96 lithostatic pressure for the purple density from c. Blue line shows that for densified crust a sill as shallow as 15 km

97 depth can supply eruptions. Schematic pressure is shown so the difference between lithostatic pressure and magma

98 pressure is visible.

99            Seismic velocities and densities beneath several LIPs are significantly higher than for  
100 typical continental crust. Figure 2c shows estimated compressional wave velocities based on a  
101 profile of crustal shear velocities beneath Deccan Traps<sup>18,19,35</sup>. Applying a standard velocity to  
102 density conversion<sup>33</sup>, we find that the densities of the upper crust are markedly greater than that  
103 of average crust (Fig. 2c). Such an upper crustal density structure means that magma from sills  
104 as shallow as ~10 km should be able to erupt. The denser crust of LIPs is likely due to basaltic  
105 crustal intrusions<sup>18,19</sup>.

106            We suggest that crustal densification due to voluminous magma intrusion and  
107 solidification is necessary to allow extrusion of continental flood basalts. The massive magma  
108 flux for a LIP is thought to originate in active upwellings of hotter-than-normal mantle<sup>36</sup>. Partial  
109 melting occurs as mantle rises and pressure decreases. The short duration of LIP magmatic  
110 events indicates that the plume-induced melt flux increases and then decreases on a time scale  
111 shorter than a few million years. The heat from the magma enables an intruded sill to heat up the  
112 overlying crust and allows rapid decrease in the intrusion depth during the phase of flux increase.  
113 As the melt flux wanes the crust above a sill should cool and the sill intrusion depth deepens.  
114 Through this shallowing and deepening cycle, dense solidified mafic intrusions are emplaced  
115 into the crust, shifting the level of eruptibility.

116            Precise controls on sill opening depths are controversial, but temperature structure is  
117 almost certain to be a critical factor. Temperature affects the strength of rocks that must be  
118 deformed to allow opening. Temperature structure also controls the rate of cooling of magma in  
119 sills. Both effects mean that the hotter the crust, the shallower the minimum depth of sill  
120 opening. Analytic relations between the heat released from intrusion and the steady-state  
121 temperature structure of the crust, described in the Methods, show that reasonable magma flux

122 variations can produce the kinds of changes in sill depth required to cause extrusion late in the  
123 emplacement of a LIP.

124 Because crustal thermal structure does not respond instantaneously to changes in  
125 magmatic heat input, we need a time-dependent model that includes diffusion and advection of  
126 heat as well as reasonable assumptions about controls on sill depth. The key question to test is  
127 whether a model can produce a major phase of extrusion starting a few hundred thousand years  
128 after the onset of detectable global warming that is caused by the CO<sub>2</sub> degassed from the  
129 preceding crustal magma intrusions.

130 Here we discuss a numerical model that builds on a recent ‘multi-sill’ approach<sup>37</sup>. The  
131 model assumes that Moho level magma reservoirs<sup>28</sup> feed crustal sill intrusions. A new feature of  
132 our model is that it explicitly determines the depth of each sill intrusion based on how earlier  
133 sills change the thermal and compositional structure of the crust. The onset of a shift of LIP  
134 magma emplacement from mostly intrusion to mostly large volume eruptions is assumed to be  
135 established when two necessary conditions are met: first, the overburden of an active sill is on  
136 average denser than melt; second, the upward migrating magma from the Moho-level reservoir  
137 and the active sill is not intruded laterally before reaching the surface. The model also assumes  
138 that the magma flux follows a Gaussian function in time and that magma solidifies shortly after  
139 emplacement. This solidification releases most CO<sub>2</sub> dissolved in the magma into the atmosphere.  
140 A standard Long-term Ocean-atmosphere-Sediment CARbon cycle Reservoir Model (LOSCAR)  
141<sup>38</sup> is used to compute the effect of this CO<sub>2</sub> flux on global temperatures (see Methods for details).

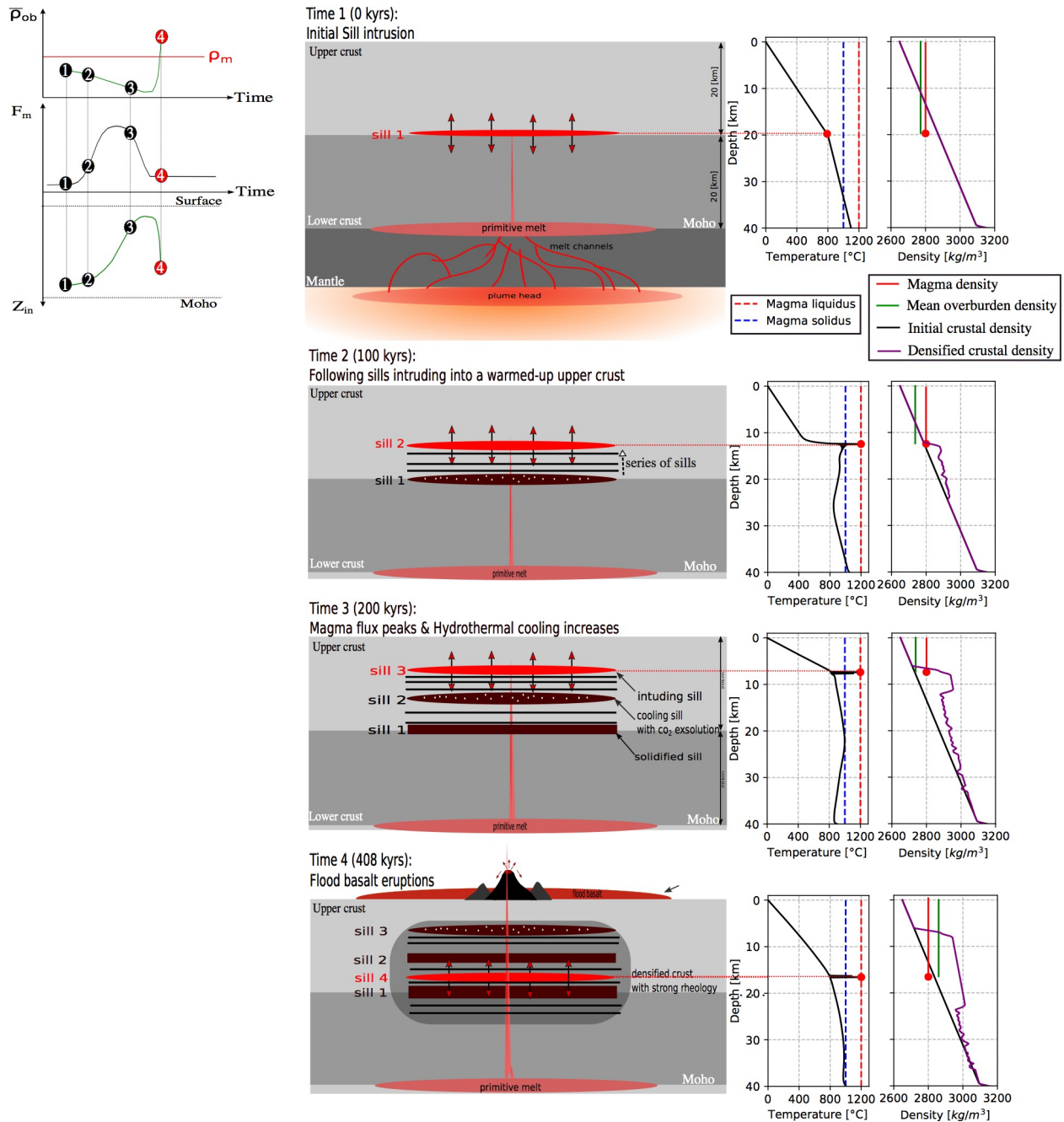
## 142 **Results**

143 The crustal magma sill intrusion system develops in four stages as illustrated in Fig. 3. At  
144 stage one, the first sills are intruded into the mid-crust, warming the country rock and densifying

145 the intruded region. As the melt supply increases, sills intrude at progressively shallower depths.  
146 The average density of the overburden of the intruding sills remains less than the magma density,  
147 so there are no major eruptions. Meanwhile, CO<sub>2</sub> exsolves from the cooling and solidifying melt  
148 and is added to the atmosphere.

149         Between stages one and two, a series of sills are emplaced upwards between ‘sill 1’ and  
150 ‘sill 2’ as melt flux increases. Significant heat is added to the crust at regions with sill intrusions.  
151 Again, there is no eruption at this time as the average density of the overburden is still less than  
152 that of magma. At stage three, as a series of sills are intruded into the mid-to-upper crust,  
153 hydrothermal circulation that transports heat to the surface increases its vigor due to the higher  
154 thermal gradient and permeability resulting from fractures induced by sill intrusions. However,  
155 the magma flux begins to decrease. Sill intrusions cannot exist shallower than the depth where  
156 heat lost to the surface is sustained by heat input from sill intrusions. Still no eruptions occur  
157 because the density of magma is still greater than the depth-averaged density of crust above the  
158 intruding sill.

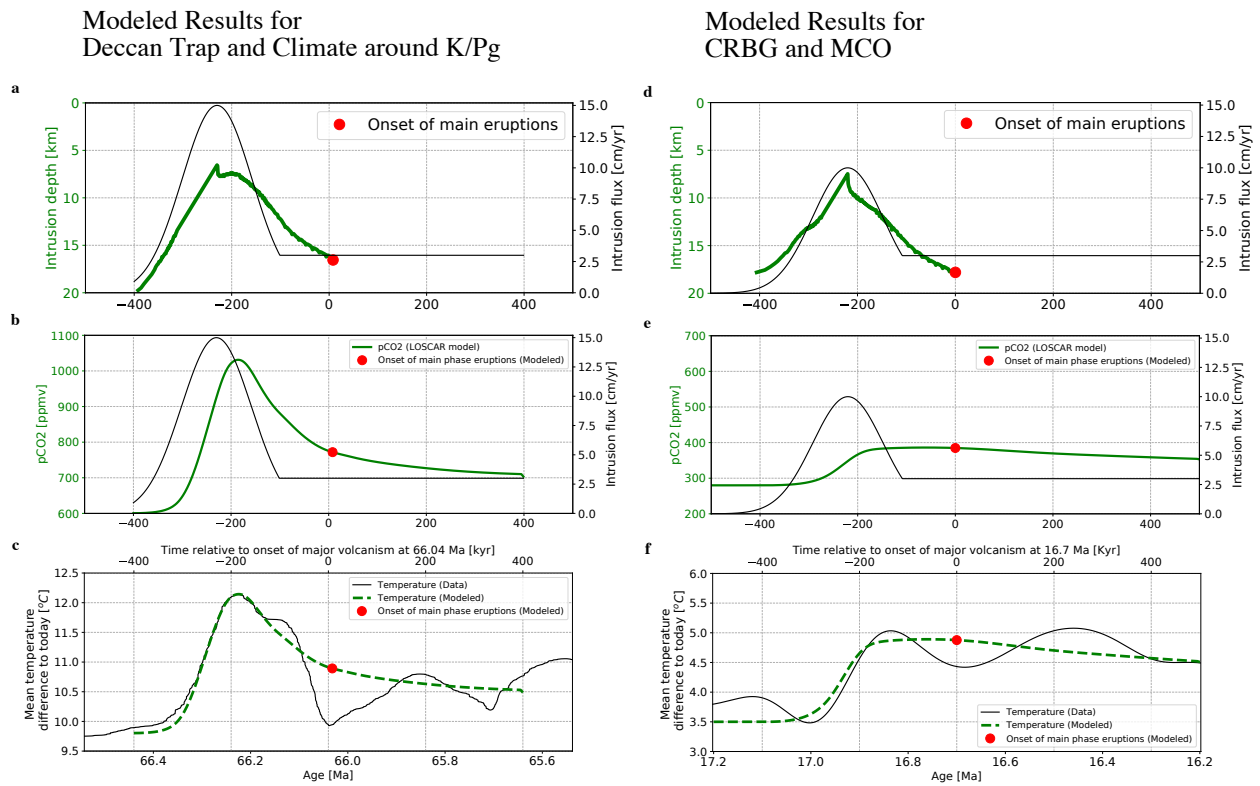
159         After several hundred thousand years of intrusion, the magma supply wanes while  
160 hydrothermal circulation is still vigorous. The intruded upper crust cools, solidifies and becomes  
161 denser and stronger. The resistance to sill intrusion increases at shallow depths. At this point  
162 (stage four), sills intrude deeper into the hotter and weaker crust (Fig.3 ‘sill 4’). The average  
163 overburden density is now higher than that of fluid magma. With the densified and stronger crust  
164 preventing lateral intrusions above the active sill, magma from the intruding sill can directly  
165 erupt to the surface.



166

167 **Fig. 3 | One dimensional thermo-mechanical model results showing the changes in crustal temperatures and**  
 168 **densities due to evolving sill intrusions.**  $Z_{in}$  is intrusion depth,  $F_m$  is magma flux,  $\bar{\rho}_{ob}$  is average density of the  
 169 overburden and  $\rho_m$  is magma density. The numbers 1 to 4 correspond to the stages of the system developments  
 170 described in the text.

171 The time lag between the onset of predicted warming and the main extrusive phase  
 172 depends on several model parameters, including: the magma flux through time; the radius of  
 173 magma sills; the initial thermal, compositional and density structures of the crust and the  
 174 efficiency of hydrothermal heat transport in the shallow crust. Without assuming vigorous  
 175 effective hydrothermal cooling of the shallow crust, the modeled time lag between intrusive and  
 176 extrusive onsets is longer than observed. Figure 4abc show results from one model run that  
 177 predicts a global warming signal similar to that seen for the Deccan Traps. The coupled  
 178 LOSCAR model indicates that the intrusive CO<sub>2</sub> initiates a ~2 degrees global warming ~300 kyr  
 179 before the major phase of LIP volcanism. By lowering the maximum intrusion flux from 15 to 10  
 180 cm/yr, increasing the upper crustal thermal gradient by 5 K/km and increasing the rate of  
 181 advective cooling by 20%, Figure 4def show results that fit the CRBG and MCO case.



183 **Fig. 4 | Time series of modeled global temperature variations and onsets of main-phase eruptions of Deccan**  
184 **Traps (abc) and CRBG (def). a,d** sill intrusion depth and the timing of transition from mostly intrusion to major  
185 phase of extrusion, predicted by the thermo-mechanical model described in the Methods, given the indicated melt  
186 flux with time. CRBG case (d) has a lower peak flux of 10 cm/yr **b,e**, global averaged atmospheric CO<sub>2</sub>  
187 concentration with time predicted by the LOSCAR climate model. **c,f** global temperature change predicted by the  
188 LOSCAR model on top of climate data (Fig.1) and with the modeled timing of onsets of main-phase eruptions.

## 189 **Discussion**

190 Our model suggests that intrusion-induced densification of the continental crust may be  
191 necessary for large-scale flood basalt eruptions. Massive CO<sub>2</sub> degassing from the solidifying  
192 intrusions can cause global warming. This provides an explanation for the decoupled climate  
193 signal and flood basalt flux. It could also help explain why the main phase of several mass  
194 extinctions predates the onset of their related LIP eruptions <sup>39</sup>.

195 Several observations support our model. A key assumption that CO<sub>2</sub> exsolves at depth as  
196 magma crystallizes is supported by recent melt inclusion studies of LIP lavas which indicates  
197 mid-to-lower crustal exsolution of abundant CO<sub>2</sub> <sup>23,40</sup>. Another requirement of the model is that  
198 magma sill intrusions should migrate upwards and downwards within several hundred thousand  
199 years to densify the crust and induce the state shift <sup>41</sup> of magma emplacements. That even  
200 modest sized mantle plumes can produce shallow magma emplacement is evidenced by seismic  
201 data indicating a large volume of partially molten crust less than 10 km below Yellowstone,  
202 where high heat flux, up to 2000 mWm<sup>-2</sup>, is also reported <sup>25</sup>.

203 Petrological and geochemical constraints, though not formally considered in the model,  
204 appear broadly consistent with our results. Analysis of the lavas of the Deccan Traps, the CRBG  
205 and some other LIPs reveal common trends of decreasing crustal contamination with time <sup>11,21,41–</sup>  
206 <sup>45</sup>. We speculate that the earlier lavas were sourced from crustal sills where mantle melt mixed

207 with continental crust, showing higher degrees of crustal contamination. In contrast, the main  
208 phase of volcanism was largely sourced directly from the deeper mantle melt reservoir, from  
209 which the magma traversed the densified and strengthened crust relatively rapidly without much  
210 interaction and hence having a stronger mantle signature <sup>11,45</sup>.

211 Many previous studies assume the main climatic effect of LIPs results from the carbon  
212 dioxide liberated by surface lava flows. Because the volume of CO<sub>2</sub> released directly from such  
213 flood basalts may be less than is needed to produce observed increases in global temperatures,  
214 several groups invoke sources of extra carbon including ‘cryptic’ degassing <sup>46</sup> either by sill  
215 intrusion heating of carbon-rich sedimentary strata <sup>24</sup> or by a carbon-rich plume melting and  
216 releasing CO<sub>2</sub> deep in the mantle <sup>47</sup>. However, besides requiring high carbon concentrations,  
217 these models either have not quantified the climatic response of the CO<sub>2</sub> release or do not explain  
218 the time lag between the global warming and the major eruption phase. As noted earlier, the  
219 volume of magma intruded deep in the crust during LIP formation may be an order of magnitude  
220 greater than that reaching the surface. Thus, the CO<sub>2</sub> released from those deep intrusions may be  
221 the main driver of the observed global warming and associated extinction events.

222 Magmatic processes are undeniably far more complex than the crude models considered  
223 here. The detailed processes of cooling, solidification and CO<sub>2</sub> degassing from large-scale crustal  
224 magma intrusions and mechanism for controlling eruption tempo of a LIP are beyond the scope  
225 of this study. We do not intend to fit the climate and extrusive data with our simple model. We  
226 merely try to provide a simple, physically-based model to show that reasonable changes in the  
227 thermal and density structures of the crust during massive magmatic events could lead to most  
228 intrusion happening before the major phase of continental flood basalt extrusions. Our results

229 support the idea that CO<sub>2</sub> from LIP intrusives is one of the main drivers of the rapid climate

230 changes causing mass extinctions.

231

232 **Main References:**

- 233 1. Courtillot, V. E. & Renne, P. R. On the ages of flood basalt events. *Comptes Rendus*  
234 *Geosci.* **335**, 113–140 (2003).
- 235 2. Coffin, M. F. & Eldholm, O. Large igneous provinces: Crustal structure, dimensions, and  
236 external consequences. *Rev. Geophys.* **32**, 1 (1994).
- 237 3. Jones, M. T., Jerram, D. A., Svensen, H. H. & Grove, C. The effects of large igneous  
238 provinces on the global carbon and sulphur cycles. *Palaeogeogr. Palaeoclimatol.*  
239 *Palaeoecol.* **441**, 4–21 (2016).
- 240 4. Sprain, C. J. *et al.* The eruptive tempo of Deccan volcanism in relation to the Cretaceous-  
241 Paleogene boundary. *Science (80-. )*. **363**, 866–870 (2019).
- 242 5. Schoene, B. *et al.* U-Pb constraints on pulsed eruption of the Deccan Traps across the end-  
243 Cretaceous mass extinction. *Science (80-. )*. **363**, 862–866 (2019).
- 244 6. Kasbohm, J. & Schoene, B. Rapid eruption of the Columbia River flood basalt and  
245 correlation with the mid-Miocene climate optimum. *Sci. Adv.* **4**, eaat8223 (2018).
- 246 7. Hull, P. M. *et al.* On impact and volcanism across the Cretaceous-Paleogene boundary.  
247 *Science (80-. )*. **367**, 266–272 (2020).
- 248 8. Holbourn, A., Kuhnt, W., Kochhann, K. G. D., Andersen, N. & Sebastian Meier, K. J.  
249 Global perturbation of the carbon cycle at the onset of the Miocene Climatic Optimum.  
250 *Geology* **43**, 123–126 (2015).
- 251 9. Westerhold, T. *et al.* An astronomically dated record of Earth’s climate and its  
252 predictability over the last 66 million years. *Science (80-. )*. **369**, 1383–1387 (2020).
- 253 10. Black, B. A. & Gibson, S. A. Deep Carbon and the Life Cycle of Large Igneous Provinces.  
254 *Elements* **15**, 319–324 (2019).

- 255 11. Richards, M. A. *et al.* Triggering of the largest Deccan eruptions by the Chicxulub impact.  
256 *Geol. Soc. Am. Bull.* **127**, 1507–1520 (2015).
- 257 12. Holbourn, A., Kuhnt, W., Kochhann, K. G. D., Andersen, N. & Sebastian Meier, K. J.  
258 Global perturbation of the carbon cycle at the onset of the Miocene Climatic Optimum.  
259 *Geology* **43**, 123–126 (2015).
- 260 13. Townsend, M., Huber, C., Degruyter, W. & Bachmann, O. Magma Chamber Growth  
261 During Intercaldera Periods: Insights From Thermo-Mechanical Modeling With  
262 Applications to Laguna del Maule, Campi Flegrei, Santorini, and Aso. *Geochemistry,*  
263 *Geophys. Geosystems* **20**, 1574–1591 (2019).
- 264 14. Ward, K. M., Zandt, G., Beck, S. L., Christensen, D. H. & McFarlin, H. Seismic imaging  
265 of the magmatic underpinnings beneath the Altiplano-Puna volcanic complex from the  
266 joint inversion of surface wave dispersion and receiver functions. *Earth Planet. Sci. Lett.*  
267 **404**, 43–53 (2014).
- 268 15. White, S. M., Crisp, J. A. & Spera, F. J. Long-term volumetric eruption rates and magma  
269 budgets. *Geochemistry, Geophys. Geosystems* **7**, 1–2 (2006).
- 270 16. Crisp, J. A. Rates of magma emplacement and volcanic output. *J. Volcanol. Geotherm.*  
271 *Res.* **20**, 177–211 (1984).
- 272 17. Ridley, V. A. & Richards, M. A. Deep crustal structure beneath large igneous provinces  
273 and the petrologic evolution of flood basalts. *Geochemistry, Geophys. Geosystems* **11**,  
274 Q09006 (2010).
- 275 18. Sen, G. & Chandrasekharam, D. Deccan Traps Flood Basalt Province: An evaluation of  
276 the thermochemical plume model. In Topics in igneous petrology (pp. 29-53). in *Topics in*  
277 *Igneous Petrology* 29–53 (Springer, Dordrecht, 2011).

- 278 19. Pandey, O. P. Deccan trap volcanic eruption affected the Archaean Dharwar craton of  
279 southern India: Seismic evidences. *J. Geol. Soc. India* **72**, 510–514 (2008).
- 280 20. Catchings, R. D. & Mooney, W. D. Crustal structure of the Columbia Plateau: Evidence  
281 for continental rifting. *J. Geophys. Res. Solid Earth* **93**, 459–474 (1988).
- 282 21. Moore, N. E., Grunder, A. L. & Bohron, W. A. The three-stage petrochemical evolution  
283 of the Steens Basalt (southeast Oregon, USA) compared to large igneous provinces and  
284 layered mafic intrusions. *Geosphere* **14**, 2505–2532 (2018).
- 285 22. Rosenthal, A., Hauri, E. H. & Hirschmann, M. M. Experimental determination of C, F,  
286 and H partitioning between mantle minerals and carbonated basalt, CO<sub>2</sub>/Ba and CO<sub>2</sub>  
287 /Nb systematics of partial melting, and the CO<sub>2</sub> contents of basaltic source regions. *Earth*  
288 *Planet. Sci. Lett.* **412**, 77–87 (2015).
- 289 23. Capriolo, M. *et al.* Deep CO<sub>2</sub> in the end-Triassic Central Atlantic Magmatic Province. *Nat.*  
290 *Commun.* **11**, 1670 (2020).
- 291 24. Svensen, H. *et al.* Release of methane from a volcanic basin as a mechanism for initial  
292 Eocene global warming. *Nature* **429**, 542–545 (2004).
- 293 25. Huang, H.-H. *et al.* The Yellowstone magmatic system from the mantle plume to the  
294 upper crust. *Science (80-. )*. **348**, 773–776 (2015).
- 295 26. Lee, H. *et al.* Massive and prolonged deep carbon emissions associated with continental  
296 rifting. *Nat. Geosci.* **9**, 145–+ (2016).
- 297 27. Mutch, E. J. F., Maclennan, J., Holland, T. J. B. & Buisman, I. Millennial storage of near-  
298 Moho magma. *Science (80-. )*. **365**, 260–264 (2019).
- 299 28. Karlstrom, L. & Richards, M. On the evolution of large ultramafic magma chambers and  
300 timescales for flood basalt eruptions. *J. Geophys. Res. Solid Earth* **116**, B08216 (2011).

- 301 29. Black, B. A. & Manga, M. Volatiles and the tempo of flood basalt magmatism. *Earth*  
302 *Planet. Sci. Lett.* **458**, 130–140 (2017).
- 303 30. Ernst, R. E., Liikane, D. A., Jowitt, S. M., Buchan, K. L. & Blanchard, J. A. A new  
304 plumbing system framework for mantle plume-related continental Large Igneous  
305 Provinces and their mafic-ultramafic intrusions. *J. Volcanol. Geotherm. Res.* **384**, 75–84  
306 (2019).
- 307 31. Hooft, E. E. & Detrick, R. S. The role of density in the accumulation of basaltic melts at  
308 mid-ocean ridges. *Geophys. Res. Lett.* **20**, 423–426 (1993).
- 309 32. Buck, W. R., Carbotte, S. M. & Mutter, C. Controls on extrusion at mid-ocean ridges.  
310 *Geology* **25**, 935 (1997).
- 311 33. Christensen, N. I. & Mooney, W. D. Seismic velocity structure and composition of the  
312 continental crust: a global view. *J. Geophys. Res.* **100**, 9761–9788 (1995).
- 313 34. Stolper, E. & Walker, D. Melt density and the average composition of basalt. *Contrib. to*  
314 *Mineral. Petrol.* **74**, 7–12 (1980).
- 315 35. Brocher, T. M. Empirical Relations between Elastic Wavespeeds and Density in the  
316 Earth's Crust. *Bull. Seismol. Soc. Am.* **95**, 2081–2092 (2005).
- 317 36. White, R. S. & McKenzie, D. Mantle plumes and flood basalts. *J. Geophys. Res. Solid*  
318 *Earth* **100**, 17543–17585 (1995).
- 319 37. Annen, C., Blundy, J. D. & Sparks, R. S. J. The Genesis of Intermediate and Silicic  
320 Magmas in Deep Crustal Hot Zones. *J. Petrol.* **47**, 505–539 (2006).
- 321 38. Zeebe, R. E., Zachos, J. C. & Dickens, G. R. Carbon dioxide forcing alone insufficient to  
322 explain Palaeocene–Eocene Thermal Maximum warming. *Nat. Geosci.* **2**, 576–580 (2009).
- 323 39. Wignall, P. B. Large igneous provinces and mass extinctions. *Earth-Science Rev.* **53**, 1–33

- 324 (2001).
- 325 40. Hernandez Nava, A. *et al.* Reconciling early Deccan Traps CO<sub>2</sub> outgassing and pre-KPB  
326 global climate. *Proc. Natl. Acad. Sci.* **118**, e2007797118 (2021).
- 327 41. Renne, P. R. *et al.* State shift in Deccan volcanism at the Cretaceous-Paleogene boundary,  
328 possibly induced by impact. *Science (80-. )*. **350**, 76–78 (2015).
- 329 42. Yu, X., Lee, C. T. A., Chen, L. H. & Zeng, G. Magmatic recharge in continental flood  
330 basalts: Insights from the Chifeng igneous province in Inner Mongolia. *Geochemistry,*  
331 *Geophys. Geosystems* **16**, 2082–2096 (2015).
- 332 43. Beane, J. E., Turner, C. A., Hooper, P. R., Subbarao, K. V. & Walsh, J. N. Stratigraphy,  
333 composition and form of the Deccan Basalts, Western Ghats, India. *Bull. Volcanol.* **48**,  
334 61–83 (1986).
- 335 44. Vanderkluysen, L., Mahoney, J. J., Hooper, P. R., Sheth, H. C. & Ray, R. The Feeder  
336 System of the Deccan Traps (India): Insights from Dike Geochemistry. *J. Petrol.* **52**, 315–  
337 343 (2011).
- 338 45. Basu, A. R., Saha-Yannopoulos, A. & Chakrabarty, P. A precise geochemical volcano-  
339 stratigraphy of the Deccan traps. *Lithos* **376–377**, 105754 (2020).
- 340 46. Armstrong McKay, D. I., Tyrrell, T., Wilson, P. A. & Foster, G. L. Estimating the impact  
341 of the cryptic degassing of Large Igneous Provinces: A mid-Miocene case-study. *Earth*  
342 *Planet. Sci. Lett.* **403**, 254–262 (2014).
- 343 47. Sobolev, S. V. *et al.* Linking mantle plumes, large igneous provinces and environmental  
344 catastrophes. *Nature* **477**, 312–316 (2011).
- 345

346 **Methods**

347 To consider the timing between flood-basalt volcanism and global climate response due  
348 to emplacement of a Large Igneous Province (LIP), we develop two versions of a thermo-  
349 mechanical sill intrusion model. For a given variable magma flux with initial crustal thermal,  
350 density and compositional structures, these models estimate temporal changes of the density and  
351 thermal structure of continental crust. These changes govern the predicted onset of the major  
352 phase of flood basalt volcanism. The model CO<sub>2</sub> degassing flux is then used as an input variable  
353 to the Long-term Ocean-atmosphere-Sediment Carbon cycle Reservoir Model (LOSCAR)<sup>38,48</sup>  
354 for its climatic response.

355 As described in the main text, a key assumption of the model is that the initiation of the  
356 major phase of flood basalt volcanism is declared when two conditions are met: first, the  
357 overburden of an active sill is on average denser than melt; second, the upward migrating magma  
358 from the shallowest active sill is not intruded laterally before reaching the surface. The first  
359 condition is determined by the crustal density structure and the depth of the intruding sill and the  
360 second condition is controlled by the thermo-mechanical state of the crust.

361 A sill intrusion of basaltic magma into continental crust affects both the thermo-  
362 mechanical state and density structure of the crust, which further affects where the following sill  
363 intrusions are most likely to happen and whether the two necessary conditions are met for large-  
364 scale flood basalt eruptions to occur. Here we first give details of a simplified analytic model and  
365 then a more complex multi-sill model that treat such intrusion-related crustal changes. The  
366 purpose of these models is to assess whether a model with reasonable assumptions and parameter  
367 values can produce significant magma intrusion followed by flood basalt eruption several  
368 hundred thousand years later. A key output is the predicted time lag between the onset of

369 significant global warming signal related to CO<sub>2</sub> release from solidifying magma intrusion and  
370 the onset of major phase of flood basalt extrusion. Before describing the simplified analytic  
371 model and the more complex multi-sill model we describe the assumptions and parameter values  
372 common to both approaches.

373

## 374 **Common Model Features**

### 375 One-dimensional Thermal Model

376 We treat crustal magma emplacement as numerous discrete basaltic sill intrusions similar  
377 to previous models<sup>37,49</sup>. We assume that each magma sill is emplaced instantly at its liquidus  
378 temperature and only account for the vertical transfer of heat, mass and stress. The assumption of  
379 instant emplacement is reasonable because thermal diffusion is much slower than the  
380 propagation of a sill intrusion. Only considering the changes in vertical z-axis direction is  
381 justifiable when a sill has a lateral dimension much larger than its thickness and depth so that the  
382 lateral heat transport is negligible. This wide but thin geometry of sills also allows us to neglect  
383 flexural response due to the loads of intrusions, which is small when compared to vertical  
384 movement of isostatic adjustment. The initial crustal thickness is taken to be close to the global  
385 average of 40 km<sup>33</sup>. The surface is always kept at 0 °C. Convection of water through pore  
386 spaces in the shallow crust is considered to enhance heat transfer and we follow other workers  
387 (refs.<sup>50,51</sup>) who approximate this effect by taking the effective conductivity of the crust to be  
388 multiplied by a factor  $Nu$  (after the Nusselt number for steady-state convection).

389 The evolution of temperatures with depth and time  $t$  are described by the one-  
390 dimensional heat equation:

$$391 \quad \frac{\partial T(z, t)}{\partial t} = Nu(z, t)\kappa \frac{\partial^2 T}{\partial z^2} - v(t) \frac{\partial T}{\partial z} + \frac{H_m}{\rho(z)C_p} \quad (1)$$

392 where  $T(z, t)$  is temperature as a function of depth  $z$  (positive downward) and time  $t$ ,  $Nu(z, t)$  is  
393 a dimensionless pre-factor describing enhanced heat transfer efficiency as a function of depth  $z$   
394 and time  $t$ , thermal diffusivity  $\kappa = 10^{-6} [m^2/s]$ ,  $v(t)$  is the downward advection velocity of  
395 crust beneath the intruding sill and is equal to the sill thickening rate  $F_m(t)$  which is also the  
396 magma supply flux per unit area.  $H_m$  with a unit of  $[W/m^3]$  is the heat liberation or storage rate  
397 which accounts for heat liberated on cooling and solidification of basaltic melt and heat stored on  
398 melting of solid basalt.  $\rho(z)$  is density and  $C_p = 1400 [J/(kg \cdot K)]$  is specific heat. The magma  
399 in sills is assumed to solidify shortly after emplacement as the time scale for thermal diffusion of  
400 a hundred-meters-thick sill is two orders of magnitude shorter than the observed time lag  
401 between onsets of warming and eruption. Here, for simplicity, we ignore the crustal radiogenic  
402 heat production.

#### 403 Assumed Magma Flux

404 The flux of magma added to the crust is taken to vary in time according to a Gaussian  
405 function with a constant tail:

$$406 \quad F_m(t) = \begin{cases} F_m^0 \exp(-(t - t_0)^2/2c^2), & t < t_1 \\ F_m^1, & t \geq t_1 \end{cases} \quad (2)$$

407 where  $F_m^0$  is the maximum flux at time  $t_0$  and  $F_m^1$  is the constant flux after time  $t_1$  when  $t > t_0$   
408 and  $F_m^0 \exp(-(t_1 - t_0)^2/2c^2) = F_m^1$ ,  $c$  controls the width in time of the Gaussian function.  
409  $F_m^0 \exp(-(t - t_0)^2/2c^2)$  represents the crustal magma intrusion flux being generated by a  
410 mantle plume head and  $F_m^1$  represents a plume tail induced magma flux. In our one-dimensional  
411 treatment the flux has units of volume flux/area ( $[m/s]$ ).

412 Assuming a radius  $R$  of the circular disk-like sill intrusions, the volume flux of magma  
413 intrusion is then easily calculated as  $V_m(t) = F_m(t)\pi R^2$ .  $R$  is assumed to be 1000 times of the

414 thickness of the sills emplaced during one modeled intrusion episode. Studies on concentrations  
415 of Ba and Nb in picrites suggest a 0.1~2 weight percent (wt%) of CO<sub>2</sub> concentration in the  
416 original mantle derived magma<sup>52,53</sup> and we here assume this concentration to be 1.5 wt% for the  
417 multi-sill model and 1.2 wt% for the analytic model, with degassing efficiencies of 55% for  
418 intrusion and 70% for extrusion<sup>10,54</sup>, depending on the timing of declaration of main phase of  
419 flood basalt eruptions, the model results in a time series of CO<sub>2</sub> outgassing flux (Fig. 4b). The  
420 modeled CO<sub>2</sub> outgassing flux is then used as an input into a multi-box long-term carbon cycle  
421 and climatic response model described below.

422         The initial density structure of continental crust  $\rho_c(z, t = 0)$  is simplified according to ref.  
423 <sup>33</sup> with a linear fit that increases from 2650 kg/m<sup>3</sup> at the surface to 3100 kg/m<sup>3</sup> at the Moho at  
424  $L_M = 40$  km (Fig. 2b). The crustal density structure  $\rho_c(z, t)$  changes with intrusions of fluid  
425 magma of 2800 kg/m<sup>3</sup> which increases to a depth dependent density  $\rho_s(z) = 2900 +$   
426  $200 \times (\frac{z}{L_M})$  kg/m<sup>3</sup> for solidified basalt (Fig. 3).

#### 427 LOSCAR climate model

428         We use the Long-term Ocean-Sediment Carbon Reservoir model (LOSCAR), v 2.0.4.3  
429 <sup>38,48</sup> to simulate the global temperature response to the CO<sub>2</sub> outgassing during LIP emplacement.  
430 Our model setup and parameters follows that of refs.<sup>7,55</sup> for the Deccan Traps case and ref<sup>46</sup> for  
431 the CRBG-MCO case. Specifically, we set [Mg<sup>2+</sup>] = 42 (46 for CRBG-MCO) mmol/kg and  
432 [Ca<sup>2+</sup>] = 21 (14.8 for CRBG-MCO) mmol/kg as equilibrium constants for carbonate chemistry  
433 calculations for K/Pg seawater. Sediment depth resolution was divided with the standard 500 m  
434 interval rather than the previously used more finely subdivided 100 m depth intervals because  
435 both show similar results but the models with a finer resolution take more than twenty times  
436 longer. The exponential constant ( $n_{si}$ ) used in the silicate weathering feedback equation was 0.6

437 (0.2 for CRBG-MCO) following refs. <sup>7,46,55</sup>. A pre-event baseline  $p\text{CO}_2$  of 600 (280 for CRBG-  
438 MCO) ppm was used after refs. <sup>7,55</sup> by restarting the model with pre-calculated steady state model  
439 parameters. The calculated global temperature response due to  $\text{CO}_2$  outgassing from the LIP  
440 emplacement is presented in Fig. 4ef of the main text. Note that exact curve fitting of the global  
441 temperature could be possible but is not the point of this study, rather, we here try to demonstrate  
442 quantitatively with reasonable and well-studied controlling parameters that our coupled sill  
443 intrusion and LOSCAR models are capable of predicting similar patterns of climate and LIP  
444 behaviors when compared to the observations.

#### 445 **Analytic sill intrusion model**

446 To demonstrate the plausibility of our conceptual model for significant intrusion before  
447 continental flood basalt extrusion we first consider a simplified analytic version based on a  
448 balance of thermal energy. The temperature structure of the crust above intruding sills is  
449 assumed to reach steady state ( $\partial T(z, t)/\partial t = 0$ ) immediately with the changes of magma supply  
450 flux. This is purely for the sake of analytic simplification and induces inaccuracy in time for  
451 temperature changes, which is treated more realistically in the multi-sill model described later.  
452 For this approach the domain of interest is between the surface and the top of an intruding sill so  
453 we neglect effects of downward crustal advection beneath the intruding sill ( $v = 0$ ). Over this  
454 domain, we only consider the liberation of heat ( $H_m/(\rho(z)C_p)$ ) from the sill as a bottom heat  
455 flux boundary condition and temperature correlates linearly with depth. The thermal equation 1  
456 is then simplified to:

$$457 \quad Nu(z, t)\kappa \frac{\partial^2 T}{\partial z^2} = 0 \quad (3)$$

458 Integrating equation 3 with respect to depth  $z$  and assuming that at the bottom boundary the heat  
459 flux ( $Q_{sill}$ ) is sourced from the cooled and solidified sill with a constant  $Nu$  yields:

460 
$$Nu \times k \frac{\partial T}{\partial z} = Q_{sill} \quad (4)$$

461 Where  $k = \kappa \rho_f C_p = 3.3$  [W/mK] is the constant thermal conductivity of crustal rocks. The heat  
 462 flux coming from the sill is taken to be:

463 
$$Q_{sill} = F_m(t) \times \rho_f (L + (T_l - T_s) C_p) \quad (5)$$

464 where  $\rho_f = 2800$  [kg/m<sup>3</sup>] is the density of the fluid magma and  $L = 4 \times 10^5$  [J/kg] is the  
 465 latent heat of solidification,  $T_s = 1000$  °C is the magma solidus and  $T_l = 1200$  °C is the magma  
 466 liquidus. Applying a top boundary condition of  $T(0, t) = 0$  °C and a moving bottom boundary  
 467 condition of  $T(Z_{in}, t) = T_s$  where  $Z_{in}$  is the evolving sill intrusion depth, we have a thermal  
 468 gradient of  $\partial T / \partial z = (T_s - T(0, t)) / Z_{in}$ , which is plugged into equation 4 and 5 to determine  
 469 the intrusion depth as:

470 
$$Z_{in} = \frac{Nu \times k \times T_s}{F_m \rho_f (L + (T_l - T_s) C_p)} \quad (6)$$

471 For the example used here we assume the plume head is controlled by  $F_m^0 =$   
 472 15 cm/yr,  $t_0 = 170$  kyrs and  $c = 210\sqrt{2/\pi}$  kyrs followed by a plume tail of constant  $F_m^1 =$   
 473 6 cm/yr thickening rate. Extended Data Fig. 1a shows this example flux-time curve and  
 474 Extended Data Fig. 1b shows the resulting variation of the intrusion depth given by equation 6.  
 475 This sill intrusion depth along with the density structure and an assumed critical overpressure for  
 476 initiation of eruptions  $\Delta P_c = 10$  MPa<sup>13,56,57</sup>, determines whether magma can extrude subaerially  
 477 or is intruded within the crust. We also assume that deepening of sill intrusions is taken to imply  
 478 replacement of felsic continental crust with denser basaltic rocks. This densification of the crust  
 479 then affects the depth where magma in a sill can be erupted which is termed as ‘level of  
 480 eruptibility’ (see main text). For extrusion to occur there has to be enough pressure in the magma  
 481 sill to drive the magma to the surface. We assume that the pressure in the magma sill is just the

482 overburden pressure:

$$483 \quad P_{OB}(Z_{in}, t) = \int_0^{Z_{in}} \rho_c(z, t) g \, dz \quad (7)$$

484 where  $\rho_c(z, t)$  is the crustal density profile. We determine the magma eruptibility by whether the  
485 magma pressure head  $P_h(z, t)$  at the surface ( $z = 0$ ) is larger than  $\Delta P_c$  when sourced from the  
486 intruding sill at depth  $Z_{in}$ , where

$$487 \quad P_h(0, t) = P_{OB}(Z_{in}, t) - \rho_f g Z_{in} \quad (8)$$

488 and this is equivalent to whether the overburden of the intruding sill is on average denser than  
489 fluid magma to an extent that:

$$490 \quad \bar{\rho}_{ob} > \rho_f + \Delta P_c / g Z_{in} \quad (9)$$

491 Where  $\bar{\rho}_{ob}$  is the average overburden density.

492 Flood basalt eruptions then could happen in two ways. If the initial sills are deeper than  
493 the level of eruptibility then the condition is met so extrusion could occur. This might only  
494 happen when the initial magma flux is low and the intrusion is deep. Alternatively, a sill can  
495 move up to a depth much shallower than the level of eruptibility and then move downward as  
496 mafic magma in the sill cools and crystallizes. The sill intrusion moves downward as the flux of  
497 magma wanes and so the heat released by the magma decreases (as indicated in Extended Data  
498 Fig. 1b). We assume that as the sill moves down it leaves behind intrusions with the density of  
499 solid basalt ( $\rho_s(z)$ ). Now the overburden will be a mix of initial low-density felsic crust and  
500 higher density solidified basalt. For a linear increase of initial crustal density with depth (Fig. 2a)  
501 eruption can happen if:

$$502 \quad Z_{in} \geq \frac{[\rho_s(Z_{inm}) + \rho_s(Z_{in}) - \rho_c(0) - \rho_c(Z_{inm})] \times Z_{inm} + 2\Delta P_c / g}{\rho_s(Z_{inm}) + \rho_s(Z_{in}) - 2\rho_f} \quad (10)$$

503 where  $Z_{inm} = \frac{Nu \times k \times T_s}{F_m^0 \rho_f (L + (T_l - T_s) C_p)}$  is the minimum depth of the sill intrusions. When this  
504 condition is met the magma pressure head at the surface is greater than  $\Delta P_c$ , the critical pressure  
505 for initiating an eruption. Extended Data Fig. 1c shows how magma pressure head varies in time.  
506 Once the timing of the onset of eruptions is determined, the model predicts a CO<sub>2</sub> degassing flux  
507 given the assumed magma concentration and degassing efficiencies. Using the CO<sub>2</sub> degassing  
508 flux as an input for the LOSCAR model we can calculate the global averaged atmospheric CO<sub>2</sub>  
509 concentration (Extended Data Fig. 1d) and temperature changes (Extended Data Fig. 1e) with  
510 time relative to the K/Pg boundary.

### 511 **Multi-sill intrusion model**

512 Our multi-sill intrusion model builds upon previous numerical studies on the genesis and  
513 evolution of evolved crustal magmas<sup>37,49</sup>. By accounting for heat transfer and mass advection  
514 during repetitive sill intrusions, such models can quantify changes in melt fraction and chemical  
515 compositions of the mantle plume induced magma that intrudes into the crust and mixes with  
516 crustal melts. As we are concerned with magma eruptibility rather than the chemical evolution of  
517 the system, our approach neglects chemical reactions of the magma and country rock. We focus  
518 on how changes in crustal temperature and composition structures control the depth of sill  
519 intrusions and the density structure of the crust.

520 We argue in the main text that the depth of sill intrusion is important for determining  
521 whether magma is emplaced as intrusions or eruptions. Some studies assume an initial intrusion  
522 depth and that subsequent sills are emplaced over, under or within the earlier sills<sup>37,49</sup>. Other  
523 studies treat sill intrusion depths through time as stochastic processes<sup>58,59</sup>. As noted below, there  
524 is considerable evidence that the thermal structure of the crust has a large influence on the depth  
525 of sill intrusion. It is also clear that sill intrusion alters the crustal temperature structure and so

526 can lead to an evolution of sill intrusion depths. Because crustal thermal structure does not  
527 respond instantaneously to changes in magmatic heat input, we derive a time dependent model  
528 that includes diffusion and advection of heat as described by equation 1. Before describing that  
529 model, we briefly review some recent studies of sill intrusion.

530         One of the most discussed ideas about sill opening depth is that magmatic sills form at  
531 the ‘level of neutral buoyancy’ (LNB) <sup>60</sup>. This model assumes that crustal density increases with  
532 depth and that magma pools at the LNB where the country rock density equals the magma  
533 density. This works in analog laboratory models only if the ‘crustal’ material has negligible  
534 strength. However, many observations are at odds with the LNB concept (see <sup>61,62</sup> and references  
535 therein). For example, this idea was tested by Hooft and Detrick <sup>31</sup> at mid-ocean ridges where  
536 seismic observations are of sufficient quality to determine the density structure above the magma  
537 filled sills. They showed that the sills were located deeper than the LNB and they suggested that  
538 the strength of cold crust may be important. Some other studies imaged sill intrusions within  
539 lower density sedimentary basins which situate shallower than the LNB (e.g. <sup>63</sup> and references  
540 therein).

541         Some previous workers focus on the effects of mechanical strength changes across layers  
542 which deflect a dike into sills and hence the sill intrusion depth is determined by the location of  
543 the layer boundary <sup>61,64</sup>. A recent analogue model study summarizes that buoyancy pressure from  
544 density contrast between host rock and the injecting fluid, rigidity contrast and lateral  
545 compression are the major controls on formation of sills <sup>65</sup>. Menand <sup>61</sup> reviewed existing models  
546 for sill emplacement depths as controlled by four major factors: (1) the buoyancy pressure due to  
547 the density contrast between host rock and injecting fluid, (2) the rigidity contrast between strata,  
548 (3) the rheology control between warm ductile material and cold brittle material, and (4) rotation

549 of deviatoric stress. These four factors can be further grouped into two major effects: either from  
550 buoyancy driving pressure controlled by density structures or effective resistant strength  
551 structure controlled by rigidity, rheology or stress state. All these factors are functions of  
552 temperature which makes sill intrusion depth strongly dependent on thermal structures.  
553 Morgan and Chen <sup>66</sup> were the first to suggest that temperature was critical in controlling the  
554 depth of magma lenses at mid-ocean ridges. A recent three-dimensional numerical modeling  
555 study of magma intrusion into the continental crust indicates that rheology and temperature of  
556 the host rocks are the key controls of how magma is emplaced <sup>67</sup>. Parsons et al. <sup>68</sup> first suggested  
557 that at large rheology contrasts where lower viscosity ductile layers are adjacent to a higher  
558 viscosity elastic layer, the least principal stress can be rotated vertically due to horizontal dike  
559 opening. This rotation of the least principal stress can arrest upward dike propagation and induce  
560 lateral sill intrusions. Similar behavior of dike arrest is described by <sup>69</sup> for rifts where lithosphere-  
561 cutting dikes stop when the ‘driving pressure’ (magma pressure minus lithospheric stress normal  
562 to the dike wall) is too small. This idea has also been used to explain analogue model results  
563 showing that horizontal compressive stress can modify the path of fluid crack from vertical to  
564 horizontal <sup>70</sup>.

565         Here, we assume that sill intrusion depth evolves with the thermo-mechanical state and  
566 density structure following previous studies of effects of thermal and stress states on sill  
567 formations <sup>66,68</sup>. For a column of magma rising through crust with density that increases with  
568 depth, the magma overpressure (magma pressure minus lithostatic pressure defined here as  
569 driving pressure  $P_d$ ) will be greatest at the level of neutral buoyancy. However, if the rocks are  
570 cold and strong at this depth the magma should not be able to force a sill to open. We estimate  
571 the resistance to sill opening as resistance pressure ( $P_r$ ).  $P_r$  depends partly on the host rock

572 temperature in that it controls whether magma will freeze before the sill intrusions can be open.  
 573  $P_r$  depends also on the composition and temperature controlling horizontal stress ( $\sigma_h(z, t)$ )  
 574 which acts normal to the vertical dike opening wall, because it controls where a vertical sill  
 575 feeding dike is stopped due to smaller driving pressure relative to that of the horizontal  
 576 compressive stress. We assume that a sill opens where the breakout pressure ( $P_{BK} = P_d - P_r$ ),  
 577 namely the difference between the driving pressure  $P_d$  and the resistance pressure  $P_r$  is the  
 578 largest as the maximum breakout pressure ( $P_{BK}(Z_{in}) = P_{BKm}$ ) (Extended Data Fig. 2).

579 The driving pressure for sill intrusion is computed by integrating density difference  
 580 between the fluid magma  $\rho_f$  and the country rock  $\rho_c$  along a vertical melt migration conduit  
 581 upward from the Moho level reservoir:

$$582 \quad P_d(z) = \int_{Z_{moho}}^z (\rho_c - \rho_f) g dz \quad (11)$$

583 This neglects any viscous pressure changes due to flow of the low viscosity primitive magma.  
 584 For the driving pressure  $P_d$ , although the density difference between fluid magma and mantle  
 585 country rock can be large, we assume the magma generated from the mantle plume gains  
 586 negligible pressure head as it percolates through the low permeability melt channels in the upper  
 587 mantle. Magma is assumed to then accumulate in the Moho-level magma reservoirs similar to  
 588 that of previous studies of continental intrusions<sup>28,29,62</sup>.

589 The resistance pressure  $P_r$  comes from two parts, namely, the thermal arrest pressure  $P_{TA}$   
 590 and the remained (un-relaxed) dike opening induced horizontal compressive stress  $\sigma_h$ .  $P_{TA}$  is the  
 591 required magma pressure for sustaining a thin but laterally wide sill intrusion. We estimate this  
 592 pressure following previous ‘thermal entry’ length calculations<sup>71,72</sup>, which consider the pressure  
 593 needed to drive magma to flow a long distance before freezing. Here, we assume a sill of

594 thickness  $w = 1$  meter and a flow distance  $R_{fz} = 200$  km before the magma fully freezes. The  
 595 magma propagation in such a sill is assumed to be simplified as a thin channel flow with an  
 596 average velocity of:

$$597 \quad \bar{u} = \frac{w^2}{12\eta_m} \frac{dP}{dx} \quad (12)$$

598 where pressure gradient  $dP/dx = P_{TA}/R_{fz}$ , assuming stable source pressure of  $P_{TA}$ <sup>73</sup> and  $\eta_m =$   
 599  $100 \text{ Pa} \cdot \text{s}$  is the assumed viscosity for fluid magma following<sup>74</sup>. Then the thermal arrest  
 600 pressure  $P_{TA}$  to drive a high aspect ratio thin channel sill intrusion before it freezes is:

$$601 \quad P_{TA} = \frac{192 \times \kappa \times \eta_m \times R_{fz}^2 \times \lambda^2}{w^4} \quad (13)$$

602 where  $\kappa$  is the thermal diffusivity. The freezing distance  $R_{fz} = \bar{u}t_{fz}$  is calculated assuming a  
 603 freezing time  $t_{fz} = w^2/(16\kappa\lambda^2)$ , which is the approximate time for a thin channel fluid magma  
 604 flow with thickness of  $w$  to freeze and  $\lambda$  is a dimensionless parameter determined by temperature  
 605 of the country rock at the sill intrusion depth  $T(Z_{in})$ <sup>72,75</sup> and is expressed in an implicit function  
 606 only solved numerically:

$$607 \quad \lambda = \frac{\exp(-\lambda^2)}{\pi^{\frac{1}{2}}S} \left[ \frac{\theta}{\text{erfc}(-\lambda)} - \frac{1-\theta}{\text{erfc}(\lambda)} \right] \quad (14)$$

608 Where dimensionless solidus temperature  $\theta = [T_s - T(Z_{in})]/[T_l - T(Z_{in})]$ , and the Stefan  
 609 number  $S = L/[C_p(T_l - T(Z_{in}))]$ , where  $T_s$  is the solidus temperature and  $T_l$  is the liquidus  
 610 temperature, here taken to be the intrusion temperature.

611 A vertical dike is assumed to propagate quasi-periodically upward to feed sill intrusions  
 612 from the magma reservoir at the base of the crust. As the dike opens it induces an instant elastic  
 613 increase in the lateral compressive stress. If the dike freezes in cold and strong crust that  
 614 behaves mainly elastically, the compressive stress increase can remain for a long period of time

615 and this should inhibit vertical propagations of later dikes. If the dike intrudes and freezes in  
616 hotter and lower viscosity crust, the initial increase in lateral compressive stress can be  
617 effectively relaxed between dike events. Following the model of Parsons et al.,<sup>68</sup> that a sill can  
618 form at brittle-ductile transitions, we calculate the second part of the model resistant pressure as  
619 the temporally variable horizontal stress  $\sigma_h(z, t)$  induced by a dike opening. Assuming the crust  
620 behaves as a Maxwell viscoelastic material<sup>73</sup> with laboratory constrained properties<sup>76,77</sup> we can  
621 estimate the amount of stress relaxation between intrusion events as functions of temperature and  
622 assumed composition. When a dike propagates vertically and opens laterally with pressure  
623 distribution of magma driving pressure  $P_d(z)$ , it induces a compressive horizontal stress  
624  $\sigma_h(z, t = 0) = P_d(z)$ , which relaxes quickly at low viscosity regions. During the quasi-periodic  
625 intersessions of  $\Delta t$  (on the order of a few thousand years depending on the magma flux) between  
626 intrusions, this initial dike induced horizontal compressive stress  $\sigma_h(z, t = 0)$  relaxed to  
627  $\sigma_h(z, t = \Delta t)$  following a Maxwell relaxation stress relation<sup>73</sup>:

$$628 \quad \sigma_h(z, t = \Delta t) = \sigma_h(z, t = 0) \exp\left(-\frac{E\Delta t}{2\mu}\right) \quad (15)$$

629 where the assumed Young's modulus  $E = 30 \text{ GPa}$ <sup>51</sup>, and the strain rate independent viscosity of  
630 the country rock  $\mu$  is calculated according to<sup>50</sup> with the power  $n = 1$ :

$$631 \quad \mu = (3A)^{-1} \times \exp\left(\frac{Q}{nRT(Z_{in})}\right) \quad (16)$$

632 where  $A$  is an empirical lab-determined viscosity pre-factor,  $Q$  is the activation energy,  $R =$   
633  $8.314 \text{ [J/(mol} \cdot \text{K)]}$  is the gas constant. For upper crust, we use lab constrained equivalent  
634 Newtonian flow rule with  $A = 0.0052 \text{ [MPa}^{-1}\text{s}^{-1}]$  (calculated from  $2/3 \times 1.57 \times (1e-3) \times 50^{0.41}$ )  
635 and  $Q = 131500 \text{ [J/mol]}$ <sup>76</sup>. For the lower crust, for simplicity,  $A$  is scaled from the upper crust  
636 value to be 5 orders of magnitude smaller and hence the resulting viscosity is 5 orders of

637 magnitude higher given the same temperature. For the 2 km of upper mantle, we apply lab-  
638 constrained Newtonian rheology from ref. <sup>77</sup> where the equivalent  $A = 0.0006 \dot{\epsilon} [MPa^{-1}s^{-1}]$   
639 (calculated from  $2/3 \times 1e6 \times (1e4)^{-3} \times 1000$ ) and  $Q = 339000 [J/mol]$ . For solidified magma,  
640 we assume its  $A$  value to be 5 orders of magnitude larger and hence the resulting viscosity is 5  
641 orders of magnitude lower than the mantle given the same temperature. To prevent numerical  
642 localizations of sill intrusion at a specific grid,  $T(Z_{in})$  is approximated with an average  
643 temperature of the country rocks near  $Z_{in}$  within a thermal diffusion length during one numerical  
644 time step of 1 Kyrs.

645 The initial vertical crustal temperature profile is taken to be piece-wise linear with the  
646 initial upper crustal thermal gradient  $dT/dZ(0 \sim 20 \text{ km}) = 40 [K/km]$  (45 [K/km] for CRBG-  
647 MCO case) and lower crustal thermal gradient  $dT/dZ(20 \sim 40 \text{ km}) = 15 [K/km]$  (Fig. 3). The  
648 magma supply flux (Fig. 4a) is assumed with  $F_m^0 = 15 [\text{cm/yr}]$  (10 [cm/yr] for CRBG –  
649 MCO case),  $t_0 = 170 [\text{kyrs}]$  and  $c = 90\sqrt{2/\pi} [\text{kyrs}]$ ,  $F_m^1 = 3 [\text{cm/yr}]$ .

650 Numerically, the heat equation 1 is discretized into a one-dimensional array of grids, and  
651 is solved by forward finite difference methods. We apply a semi-Lagrangian Crank-Nicolson  
652 algorithm <sup>78</sup>, which is coupled with one-half backward implicit step <sup>79</sup> to damp the Crank-  
653 Nicolson error oscillations introduced by sharp temperature corners from sill intrusions. As noted  
654 above, the average effect of hydrothermal circulation is simulated by increasing the thermal  
655 diffusivity  $\kappa$  by a factor of  $Nu$ . The efficiency of hydrothermal circulation should scale with  
656 crustal permeability and thermal gradient. Hence it should depend on the existence of  
657 interconnected cracks as well as the crustal thermal condition. Upper crustal thermal gradient and  
658 fracture events should peak around the time when the magma flux  $F_m(t)$  maximizes at  $t_0$ . Hence,  
659 we assume  $Nu = 25$  from the surface to 20 km when  $t \geq t_0$  and  $Nu = 1$  otherwise ( $Nu =$

660 30 for CRBG-MCO case). Note that measurements from Yellowstone indicate up to 2000 mWm<sup>-2</sup>  
661 of surface heat flux <sup>25</sup>, which is nearly 30 times of that of normal continental crust of 65 mWm<sup>-2</sup>  
662 <sup>73</sup>.

663 We determine the magma eruptibility by whether the magma pressure head at the surface  
664 ( $P_h(0) = \int_{Z_{in}}^0 (\rho_c - \rho_f)g dz$ ) is larger than the critical pressure ( $\Delta P_c$ ) for initiating an eruption  
665 when sourced from the intruding sill at depth  $Z_{in}$ :

$$666 \quad P_h(0) > \Delta P_c \quad (17)$$

667 This is equivalent to considering whether the average density of the overburden of an intruding  
668 sill is larger than the density of fluid magma to an extent of equation 9. During the initial phases  
669 when the sill is deep or when the crust densifies due to sill intrusions, magma driving pressure at  
670 the surface  $P_d(0)$  can be positive, which means magma from the Moho reservoir has the  
671 potential to erupt. However, we do not count major phase of flood basalts eruptibility when  
672 magma is sourced from the Moho reservoir during the early phase of an LIP emplacement  
673 because the pressure head should be consumed by lateral sill intrusions into the initial weaker  
674 and lower density crust before magma can reach the surface. We do not consider viscous  
675 resistances for sill or dike intrusions as they are negligible compared to the thermal arrest  
676 resistance from sill intrusions <sup>74</sup>. We also neglect temporal variations in elastic overpressure from  
677 the magma reservoir which can be responsible for finer time scale hiatuses in magma eruptions  
678 <sup>28,29</sup>.

679 We also include in the supplementary information with eight videos of the multi-sill  
680 intrusion models (Video 1 to 4 for the Deccan case and Video 5 to 8 for the CRB case), which  
681 illustrate in detailed the changes in crustal density, temperature, pressures, viscosity and sill  
682 intrusion depths due to repetitive sill intrusions. Video 1 and 5 show the crustal densification

683 process for comparison to the data in Fig. 2F. Video 2 and 6 present the crustal temperature and  
684 pressures evolution. Note that for the assumed rheology parameters the thermal arrest resistance  
685 pressure has the dominant effect on controlling sill intrusion depths when the sills are moving  
686 upwards into weak lower part of the upper crust, but the dike related stress change becomes  
687 important during the sill-deepening phase (starting ~175 kyr for video 2) as the sills open into  
688 stronger mafic intrusives. Video 3 and 7 show the variations in temperature and viscosity  
689 structure resulted from the assumed lab-constrained rheological parameters. Video 4 and 8  
690 include changes in sill intrusion depth, temperature, magma overpressure, magma breakout  
691 pressure and magma overpressure if sourced from the intruding sill. With our model formulation,  
692 the intruding depth is determined by considering both the density structure and the thermo-  
693 mechanical conditions and hence is not always at the level of neutral buoyancy.

694

695 **Data availability:** For Fig. 1, global temperature change data are from ref. <sup>7</sup> (DOI:  
696 10.1126/science.aay5055) and Deccan Trap extrusive flux data are converted from ref. <sup>4</sup> (DOI:  
697 10.1126/science.aav1446). For Fig. 2, Seismic velocity data are converted from refs. <sup>19,33</sup>.  
698 **Code availability:** All codes for our numerical calculations are available from X.T. upon request.

699 **Methods References:**

- 700 48. Zeebe, R. E. LOSCAR: Long-term Ocean-atmosphere-Sediment Carbon cycle Reservoir  
701 Model v2.0.4. *Geosci. Model Dev.* **5**, 149–166 (2012).
- 702 49. Solano, J. M. S., Jackson, M. D., Sparks, R. S. J., Blundy, J. D. & Annen, C. Melt  
703 Segregation in Deep Crustal Hot Zones: a Mechanism for Chemical Differentiation,  
704 Crustal Assimilation and the Formation of Evolved Magmas. *J. Petrol.* **53**, 1999–2026  
705 (2012).
- 706 50. Chen, Y. & Morgan, W. J. A nonlinear rheology model for mid-ocean ridge axis  
707 topography. *J. Geophys. Res.* **95**, 17583 (1990).
- 708 51. Behn, M. D. & Ito, G. Magmatic and tectonic extension at mid-ocean ridges: 1. Controls  
709 on fault characteristics. *Geochemistry, Geophys. Geosystems* **9**, n/a-n/a (2008).
- 710 52. Kent, A. J. R. *et al.* Mantle heterogeneity during the formation of the North Atlantic  
711 Igneous Province: Constraints from trace element and Sr-Nd-Os-O isotope systematics of  
712 Baffin Island picrites. *Geochemistry, Geophys. Geosystems* **5**, n/a-n/a (2004).
- 713 53. Sobolev, A. V., Krivolutsкая, N. A. & Kuzmin, D. V. Petrology of the parental melts and  
714 mantle sources of Siberian trap magmatism. *Petrology* **17**, 253–286 (2009).
- 715 54. Hartley, M. E., MacLennan, J., Edmonds, M. & Thordarson, T. Reconstructing the deep  
716 CO<sub>2</sub> degassing behaviour of large basaltic fissure eruptions. *Earth Planet. Sci. Lett.* **393**,  
717 120–131 (2014).
- 718 55. Henehan, M. J., Hull, P. M., Penman, D. E., Rae, J. W. B. & Schmidt, D. N.  
719 Biogeochemical significance of pelagic ecosystem function: an end-Cretaceous case study.  
720 *Philos. Trans. R. Soc. B Biol. Sci.* **371**, 20150510 (2016).
- 721 56. Rubin, A. M. Getting granite dikes out of the source region. *J. Geophys. Res. Solid Earth*

- 722           **100**, 5911–5929 (1995).
- 723 57. Jellinek, A. M. & DePaolo, D. J. A model for the origin of large silicic magma chambers:  
724           Precursors of caldera-forming eruptions. *Bull. Volcanol.* **65**, 363–381 (2003).
- 725 58. Karakas, O., Degruyter, W., Bachmann, O. & Dufek, J. Lifetime and size of shallow  
726           magma bodies controlled by crustal-scale magmatism. *Nat. Geosci.* **10**, 446–450 (2017).
- 727 59. Dufek, J. & Bergantz, G. W. Lower Crustal Magma Genesis and Preservation: a  
728           Stochastic Framework for the Evaluation of Basalt–Crust Interaction. *J. Petrol.* **46**, 2167–  
729           2195 (2005).
- 730 60. Ryan, M. P. Neutral buoyancy and the mechanical evolution of magmatic system. *Magmat.*  
731           *Process Physicochem. Princ.* 259–287 (1987).
- 732 61. Menand, T. Physical controls and depth of emplacement of igneous bodies: A review.  
733           *Tectonophysics* **500**, 11–19 (2011).
- 734 62. Rohrman, M. Intrusive large igneous provinces below sedimentary basins: An example  
735           from the Exmouth Plateau (NW Australia). *J. Geophys. Res. Solid Earth* **118**, 4477–4487  
736           (2013).
- 737 63. Magee, C. *et al.* Lateral magma flow in mafic sill complexes. *Geosphere* **12**, 809–841  
738           (2016).
- 739 64. Menand, T. The mechanics and dynamics of sills in layered elastic rocks and their  
740           implications for the growth of laccoliths and other igneous complexes. *Earth Planet. Sci.*  
741           *Lett.* **267**, 93–99 (2008).
- 742 65. Sili, G., Urbani, S. & Acocella, V. What Controls Sill Formation: An Overview From  
743           Analogue Models. *J. Geophys. Res. Solid Earth* **124**, 8205–8222 (2019).
- 744 66. Morgan, J. P. & Chen, Y. J. The genesis of oceanic crust: Magma injection, hydrothermal

- 745 circulation, and crustal flow. *J. Geophys. Res.* **98**, 6283 (1993).
- 746 67. Gorczyk, W. & Vogt, K. Intrusion of Magmatic Bodies Into the Continental Crust: 3-D  
747 Numerical Models. *Tectonics* **37**, 705–723 (2018).
- 748 68. Parsons, T., Sleep, N. H. & Thompson, G. A. Host rock rheology controls on the  
749 emplacement of tabular intrusions: Implications for underplating of extending crust.  
750 *Tectonics* **11**, 1348–1356 (1992).
- 751 69. Buck, W. R. The role of magma in the development of the Afro-Arabian Rift System.  
752 *Geol. Soc. London, Spec. Publ.* **259**, 43–54 (2006).
- 753 70. Menand, T., Daniels, K. A. & Benghiat, P. Dyke propagation and sill formation in a  
754 compressive tectonic environment. *J. Geophys. Res.* **115**, B08201 (2010).
- 755 71. Spence, D. A. & Turcotte, D. L. Magma-driven propagation of cracks. *J. Geophys. Res.*  
756 *Solid Earth* **90**, 575–580 (1985).
- 757 72. Fialko, Y. A. & Rubin, A. M. Thermodynamics of lateral dike propagation: Implications  
758 for crustal accretion at slow spreading mid-ocean ridges. *J. Geophys. Res. Solid Earth* **103**,  
759 2501–2514 (1998).
- 760 73. Turcotte, D. L. & Schubert, G. *Geodynamics*. (Cambridge University Press, 2002).  
761 doi:10.1017/CBO9780511807442
- 762 74. Lister, J. R. & Kerr, R. C. Fluid-mechanical models of crack propagation and their  
763 application to magma transport in dykes. *J. Geophys. Res.* **96**, 10049 (1991).
- 764 75. Carslaw, H. S. & Jaeger, J. C. *Conduction of Heat in Solids*. (Oxford University Press,  
765 1959).
- 766 76. Wang, J. N., Hobbs, B. E., Ord, A., Shimamoto, T. & Toriumi, M. Newtonian Dislocation  
767 Creep in Quartzites: Implications for the Rheology of the Lower Crust. *Science (80-. )*.

- 768           **265**, 1204–1206 (1994).
- 769   77.   Hirth, G. & Kohlstedt, D. Rheology of the upper mantle and the mantle wedge: A view  
770           from the experimentalists. *Geophys. Monogr. Ser.* **138**, 83–105 (2003).
- 771   78.   Spiegelman, M. & Katz, R. F. A semi-Lagrangian Crank-Nicolson algorithm for the  
772           numerical solution of advection-diffusion problems. *Geochemistry, Geophys. Geosystems*  
773           **7**, (2006).
- 774   79.   Britz, D., Østerby, O. & Strutwolf, J. Damping of Crank-Nicolson error oscillations.  
775           *Comput. Biol. Chem.* **27**, 253–263 (2003).
- 776   80.   Schoene, B. *et al.* An evaluation of Deccan Traps eruption rates using geochronologic data.  
777           *Geochronol. Discuss.* (2020). doi:<https://doi.org/10.5194/gchron-2020-11>
- 778   81.   D’Hondt, S. & Lindinger, M. A stable isotopic record of the Maastrichtian ocean-climate  
779           system: South Atlantic DSDP site 528. *Palaeogeogr. Palaeoclimatol. Palaeoecol.* **112**,  
780           363–378 (1994).

781   **Acknowledgments:** This work greatly benefited from discussions with Eunseo Choi, Jean-  
782   Arthur Olive, William Ryan, Elizabeth Fischer and Courtney Sprain. We thank reviewers  
783   Jennifer Kasbohm, Jon Blundy, Mark Richards and Tushar Mittal for their meticulous and  
784   constructive reviews. We also thank Richard Zeebe for sharing the LOSCAR code. This work is  
785   supported by NSF grants OCE-1654745.

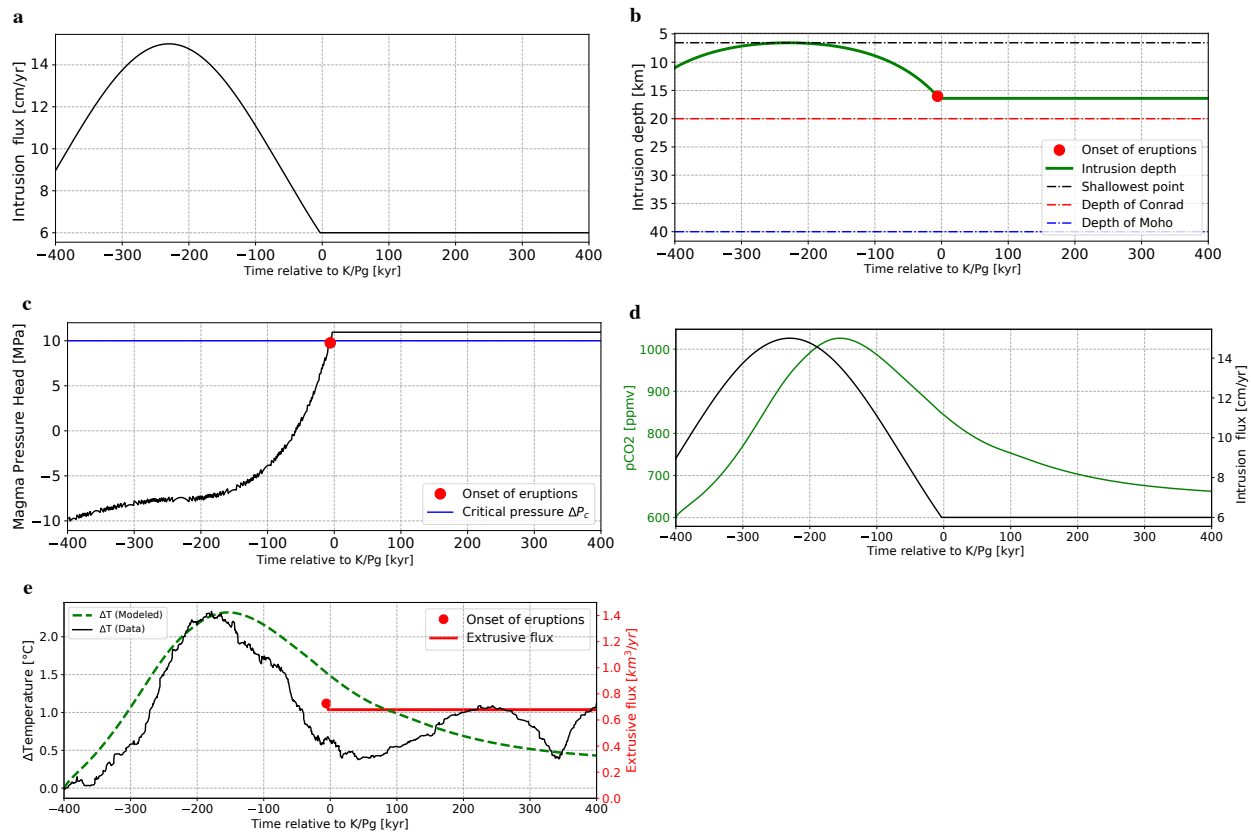
786   **Author contributions:** X.T., advised by W.R.B., conducted the model experiments and both  
787   authors wrote the manuscript.

788   **Competing interests:** Authors declare no competing interests.

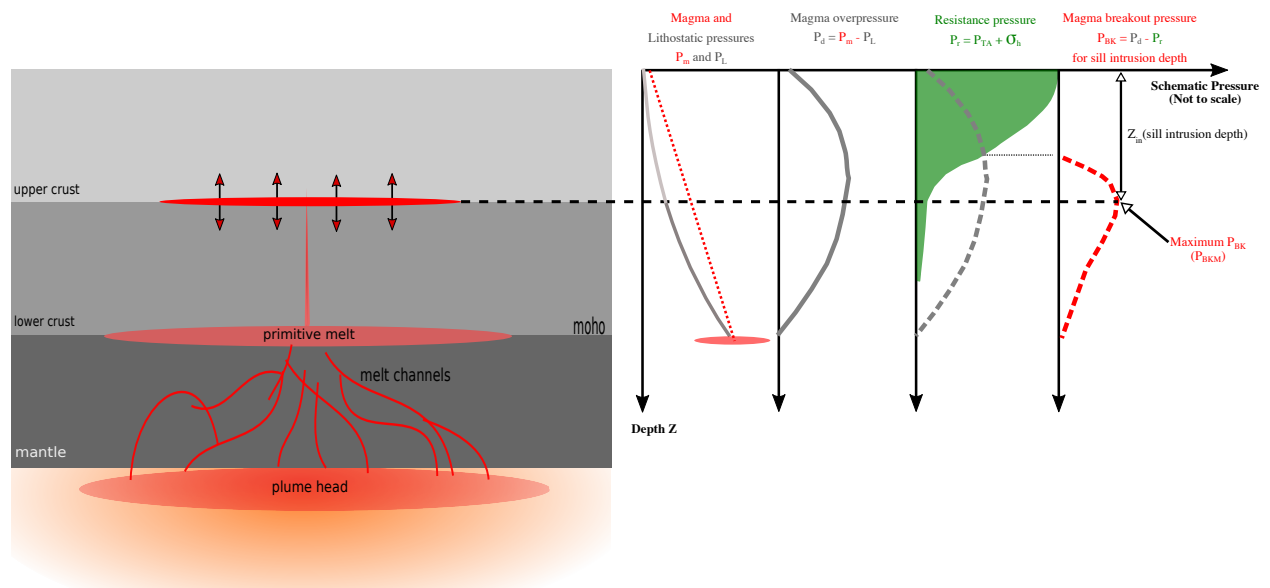
789   **Additional information**

790   **Supplementary information** of four videos is available for this paper.

791 **Correspondence and requests for materials** should be addressed to X. T. at email address:  
 792 [xtian@ldeo.columbia.edu](mailto:xtian@ldeo.columbia.edu).



793  
 794 **Extended Data Fig. 1 | Example of the steady-state analytic model results as functions of time relative to the**  
 795 **Cretaceous-Paleogene (K/Pg) boundary. a,** Assumed Gaussian sill opening flux in terms of magma volume flux  
 796 per unit area of the sill. **b,** Sill intrusion depth for the melt flux of (a) and the thermal energy balance of equation (6).  
 797 **c,** Magma pressure head at the surface sourced from the intruding sill. Magma eruption is possible when this  
 798 pressure equals to the critical pressure  $\Delta P_c$  at around K/Pg. For this case, magma flux from -400 kyrs to 0 kyrs is  
 799 intruded. **d,** global averaged atmospheric CO<sub>2</sub> concentration with time predicted by the LOSCAR climate model. **e,**  
 800 global temperature change predicted by the LOSCAR model along with the extrusive flux with time to compare with  
 801 the observation in Fig. 1a.

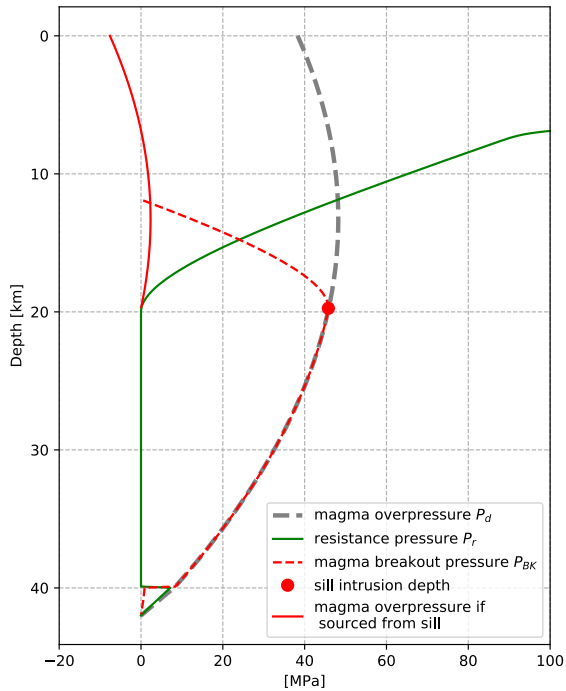


802

803 **Extended Data Fig. 2 | Schematic illustrations of how to determine the depth for a sill intrusion at maximum**  
 804 **breakout pressure. Magma overpressure ( $P_d$ ), resistance pressure ( $P_r$ ) and magma breakout pressure ( $P_{BK}$ )**  
 805 **for determining sill intrusion depth ( $Z_{in}$ ).**

806

807 **Supplementary Information Video 1 and 5 | Video for modeled changes in crustal density due to evolving sill**  
 808 **intrusions.** Model time is shown at the upper left. Green line shows the extent and value of the averaged overburden  
 809 density. Purple line shows the evolving crustal densities due to sill intrusions. The red dot indicates the sill intrusion  
 810 depth and the magma density. The dashed grey line shows the initial crustal density profile.



811

812

813 **Supplementary Information Video 2 and 6 | Video for modeled changes in temperature and pressures due to**  
 814 **evolving sill intrusions.** Model time is shown at the upper left. Left panel: temperature changes due to sill intrusions.  
 815 The blue and red dashed lines indicate magma solidus and liquidus respectively. Right panel: changes in pressures  
 816 due to sill intrusions (initial condition and legends are shown as the figure above: the dashed grey line is for the  
 817 magma overpressure (driving pressure  $P_d$ ). The green line is for the resistance pressure  $P_r$ . The dashed red line is for  
 818 the magma breakout pressure  $P_{BK}$ . The solid red line is for the magma overpressure if sourced from the intruding sill.  
 819 Red dots indicate depth of sill intrusions).

820 **Supplementary Information Video 3 and 7 | Video for modeled changes in temperature and viscosity due to**  
 821 **evolving sill intrusions.** Model time is shown at the upper left. Left panel: temperature changes due to sill intrusions.  
 822 The blue and red dashed lines indicate magma solidus and liquidus respectively. Right panel: the dashed grey line is  
 823 for the initial viscosity. The solid line is for the evolving viscosity structure. Red dots indicate depth of sill intrusions.

824 **Supplementary Information Video 4 and 8 | Video for modeled changes in sill depths, temperature and**  
 825 **magma pressures due to evolving sill intrusions.** Model time is shown at the lower left. Top panel: sill intrusion  
 826 depth given the melt flux with time. Lower left panel: temperature changes due to sill intrusions. The blue and red  
 827 dashed lines indicate magma solidus and liquidus respectively. Lower right panel: the dashed grey line is for the

828 magma overpressure (driving pressure  $P_d$ ). The dashed red line is for the magma breakout pressure  $P_{BK}$ . The solid  
829 red line is for the magma overpressure if sourced from the intruding sill. Red dots indicate depth of sill intrusions.

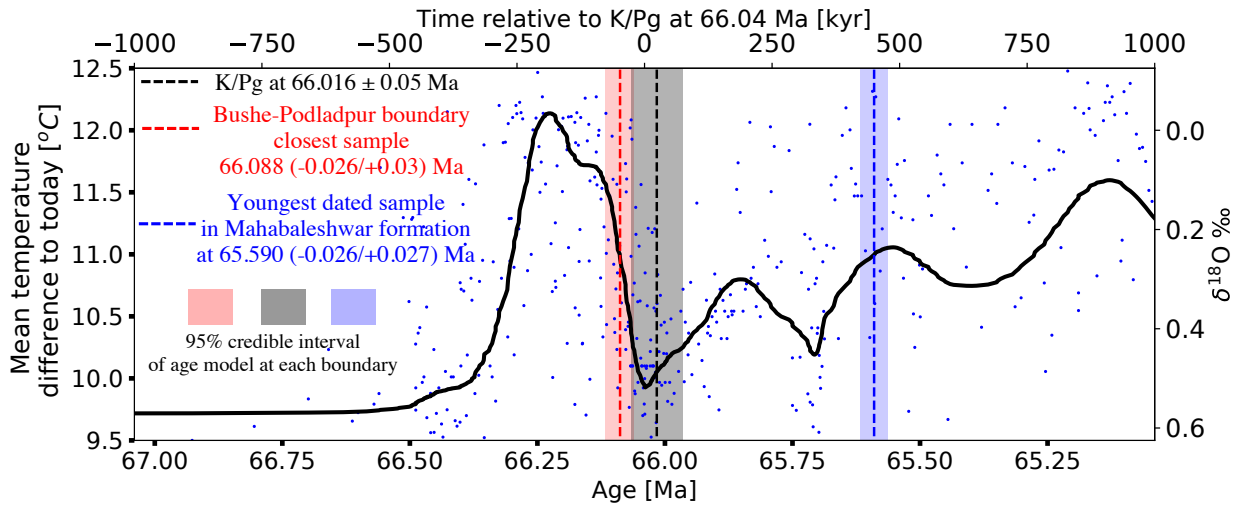
830 **Discussion on differences in geochronology age models for Deccan Traps**

831

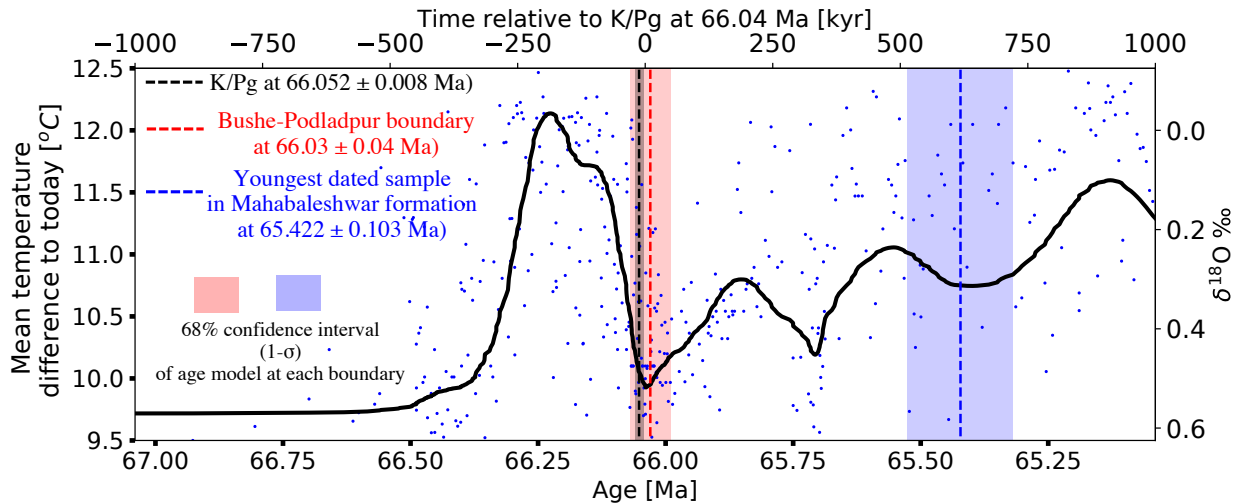
832 Two very different approaches to estimating the ages of the basalts of the Deccan traps  
833 have been reported in recent years and they give somewhat different estimates of those ages. Age  
834 model 1 (M1) from Schoene et al., (2019)<sup>5</sup> used U-Pb geochronology by isotope dilution–  
835 thermal ionization mass spectrometry, which provides analytical uncertainties ( $\pm 2\sigma$ ) as low as  
836 40,000 years for individual dated zircons. Schoene et al., (2019) sampled both coarse-grained  
837 basalts and sedimentary beds between basalt flows that infrequently contain zircon-bearing  
838 volcanic ashes. Age model 2 (M2) from Sprain et al., (2019)<sup>4</sup> used what they describe as “high-  
839 resolution  $^{40}\text{Ar}/^{39}\text{Ar}$  plagioclase ages from the Deccan Traps that locate the K/Pg and better refine  
840 the timing and tempo of eruptive fluxes.”

841 Schoene et al., (2020)<sup>80</sup> describe a detailed comparison between the two age models for  
842 Deccan Trap volcanism and show that the models give essentially consistent results. In Figure  
843 S1, we illustrate the two model results. That figure shows three major differences between M1  
844 and M2 models. Relative to M2 model M1 indicates: (1) a ~36 kyr younger, K/Pg boundary; (2)  
845 a ~58 kyr older a Bushe-Podladpur formation boundary; and (3) that the youngest sample in the  
846 Mahabaleshwar formation is ~168 kyr older. However, these finer differences wouldn't change  
847 the first order observation that the onset of global warming at ~66.4 Ma is about 360 kyrs prior  
848 to the onset of 73% of total volume of Deccan Traps eruptions at the Bushe-Podladpur formation  
849 boundary.

a. age model M1 (Schoene et al., 2019)



b. age model M2 (Sprain et al., 2019)



850

851 **Supplementary Figure S1. Comparison between age models M1 and M2 for Deccan Traps and K/Pg climate**

852 **variations.** Both age models of Deccan Traps use Richards et al., (2015)<sup>11</sup> flood basalt volume model in which the 3  
853 formations (Poladpur, Ambenali and Mahabaleshwar) in the younger Wai subgroup comprise a volume of about  
854 439,000 km<sup>3</sup>, 73% of total volume (602,700 km<sup>3</sup>) of Deccan Traps. Both age models are overlapped with global  
855 climate change data from Hull et al., (2020)<sup>7</sup>, which use 66.04 Ma as K/Pg boundary from D'Hondt and Lindiger  
856 (1994)<sup>81</sup>.  $\Delta$ Temperature in Fig.1 of Hull et al., (2020) is the global temperature change relative to the temperature at  
857 K/Pg boundary. We assume a temperature of 10.1°C at 66.040242 Ma for temperature at the K/Pg boundary  
858 provided by Table S4 of Hull et al., (2020) citing Li and Keller (1998). This allow us to calculate temperature  
859 difference to today applying equations from Table S7 of Westerhold et al., (2020). See Hull et al., (2020) for the

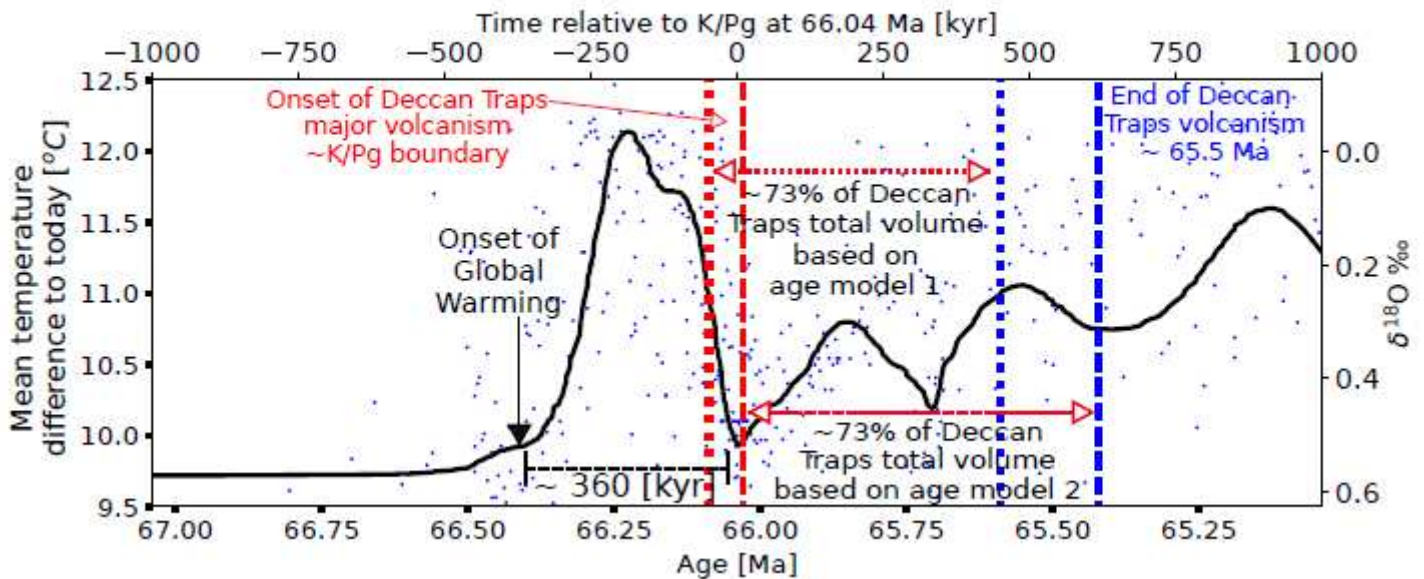
860 data detailed description. We filter data from Table S4 of Hull et al., (2020) with a Butterworth low pass filter  
861 (scipy.signal.butter) with the order of the filter  $N=6$  and the critical frequency parameter  $W_n = 0.01$ . The  $\delta^{18}O$  is  
862 converted from the temperature data using equations from Table S7 of Westerhold et al., (2020). a): age model M1  
863 from Schoene et al., 2019. The black dashed-line is the model preferred K/Pg boundary at  $66.016 \pm 0.05$  Ma with 95%  
864 credible interval indicated with the gray rectangle. The red dashed-line is the model preferred Bushe-Poladpur  
865 formation boundary at  $66.088 (-0.026/+0.03)$  Ma with 95% credible interval indicated with the red rectangle. The  
866 blue dashed-line is the model preferred youngest dated sample in Mahabaleshwar formation at  $65.590 (-0.026/+0.027)$   
867 Ma with 95% credible interval indicated with the blue rectangle. b): age model M2 from Sprain et al., 2019. The  
868 black dashed-line is the model preferred K/Pg boundary at  $66.052 \pm 0.008$  Ma. The red dashed-line is the model  
869 preferred Bushe-Poladpur formation boundary at  $66.03 \pm 0.04$  Ma with  $1-\sigma$  (68%) confidence interval indicated with  
870 the red rectangle. The blue dashed-line is the model preferred youngest dated sample in Mahabaleshwar formation at  
871  $65.422 \pm 0.103$  Ma with  $1-\sigma$  (68%) confidence interval indicated with the blue rectangle.

872

873         The Schoene et al., (2019) M1 age model resolves a finer eruption flux that has four  
874 separate pulses including one that is 20 to 60 kyr prior to the impact (K/Pg boundary). However,  
875 according to Hull et al., (2020), when assuming an eruption flux according to the M1 flux model  
876 from Schoene et al., (2019), which is the case 3 (punctuated) of Hull et al., 2020 climate  
877 modeling, the modeled climate response is not able to reproduce the observed globally compiled  
878 climate change data. Hull et al., (2020) suggest that “if the M1 model from Schoene is correct  
879 with a large pulse of emplacement 20 to 60 kyr before the impact (K/Pg boundary), then most  
880  $CO_2$  outgassing must have preceded lava emplacement by several hundred thousand years. This  
881 would be before the eruption of the most voluminous stages of Deccan volcanism (i.e. before the  
882 Wai group starting at Bushe-Podladpur formation boundary) ”

# Figures

## a Deccan Traps and K/Pg Global Warming



## b Columbia River Basalt Group (CRBG) and Miocene Climate Optimum (MCO)

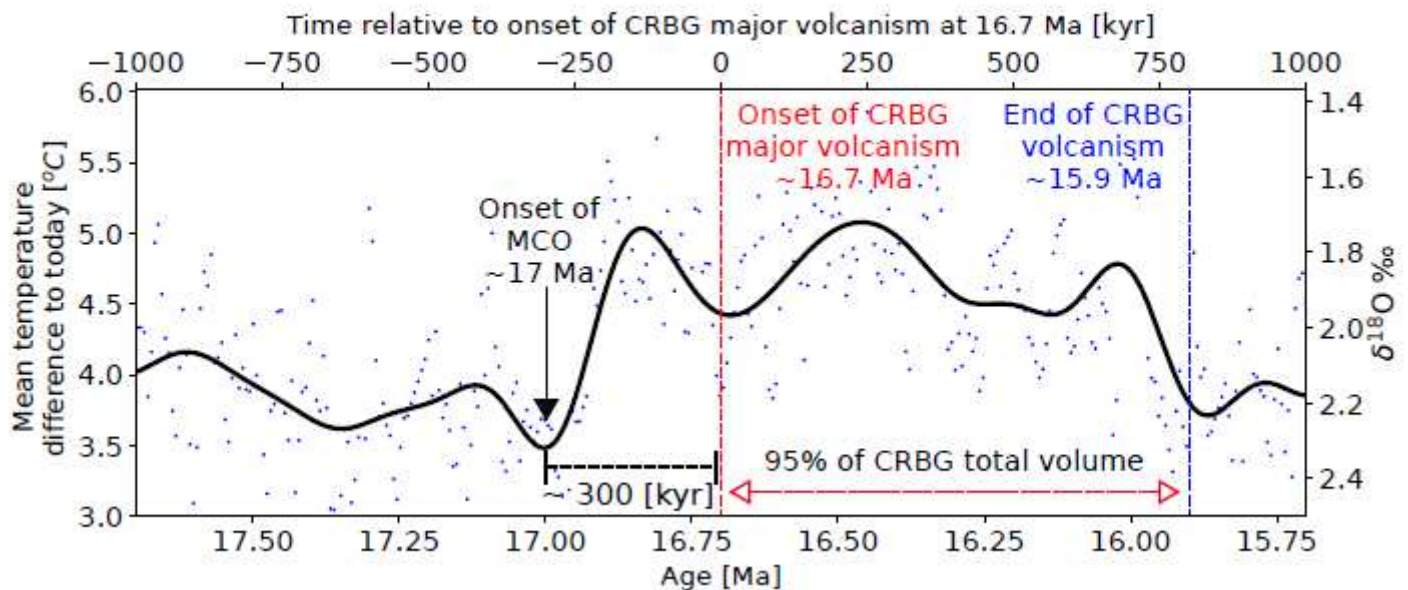
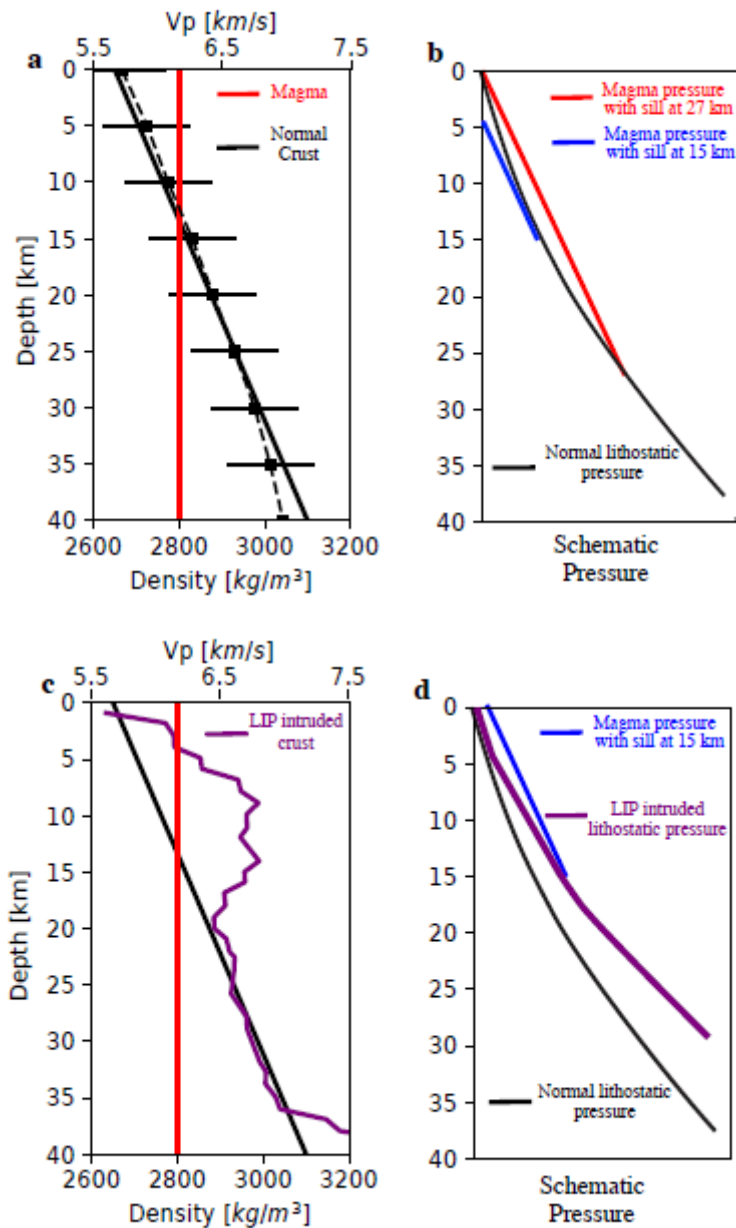


Figure 1

Global temperature variations within 1000 kyr of the approximate onset of the main volcanic phases of the Deccan Traps<sup>4,5</sup> and Columbia River Basalt Group<sup>6</sup> LIPs. Black lines result from low-pass filtering of the blue dots  $\delta^{18}\text{O}$  data and estimated temperature variations with time<sup>7–9</sup>. The age of onset and ending of the main Deccan volcanic phase for two basalt dating methods are indicated by the pairs of vertical dashed lines. Vertical arrows indicate that the onset of global warming for each case precedes

the main volcanic phase by ~ 300 kyr. Details of the age models and temperature estimates are described in the supplement.



**Figure 2**

Illustrations of relations between seismic velocities, densities and pressures in typical continental crust (a,b) and the crust under part of the Deccan LIP (c,d). a, shows average continental P-wave velocity (dashed) from ref. ^33 with density assuming a linear relation between velocity and density. Solid lines show densities assumed in the model. Magma density is from ref. ^34. b, black line shows lithostatic pressure for the density structure given by solid line in a. Red line shows static pressure in a column of magma just reaching the surface while blue shows the same for a column of magma with lithostatic pressure at 15 km depth. c, P-wave velocity and density profiles beneath Deccan Traps are converted from refs. ^18,19 using a  $V_s$  to  $V_p$  relationship (ref. ^35). d, Purple line shows lithostatic pressure for the

purple density from c. Blue line shows that for densified crust a sill as shallow as 15 km depth can supply eruptions. Schematic pressure is shown so the difference between lithostatic pressure and magma pressure is visible.

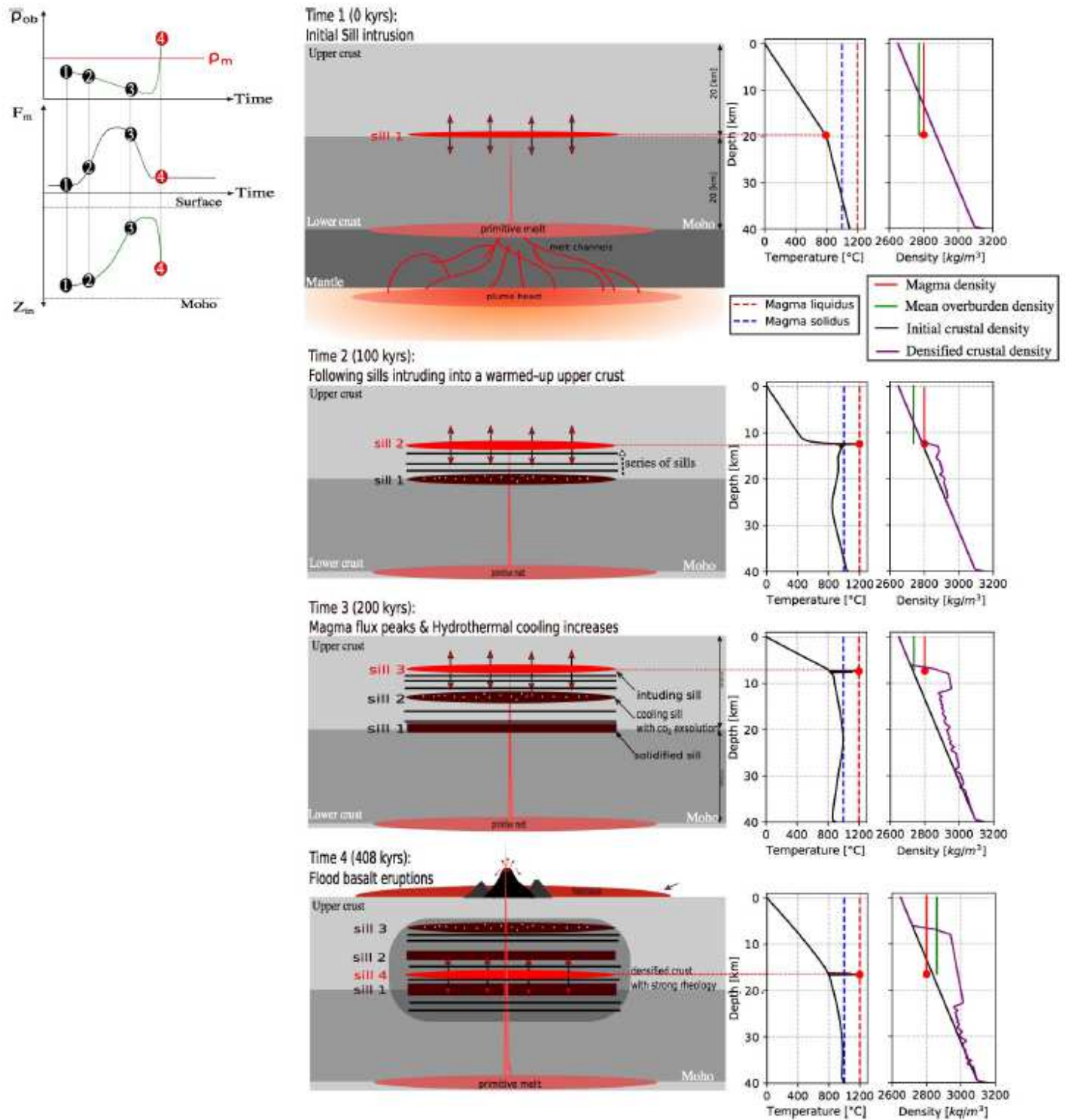
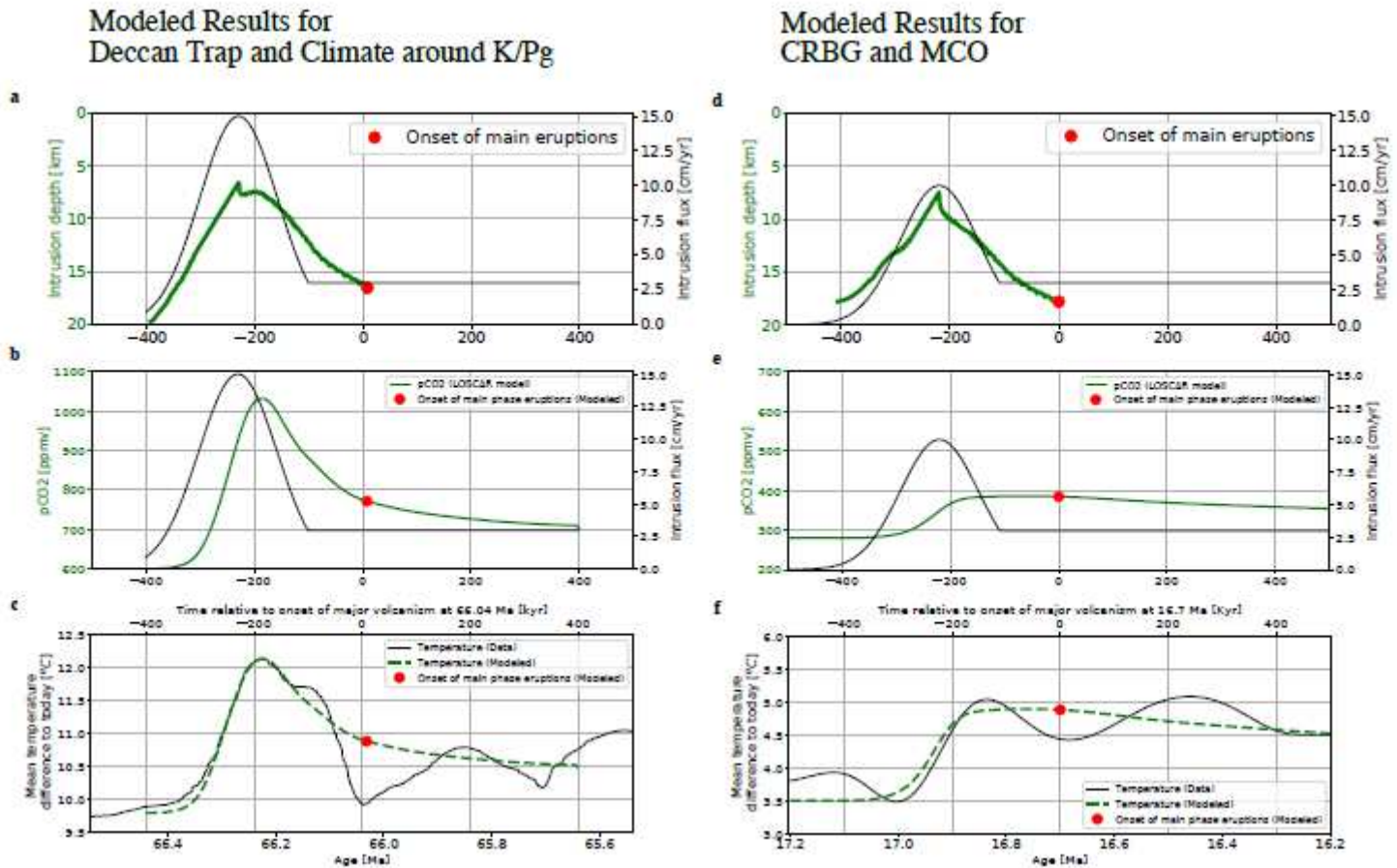


Figure 3

One dimensional thermo-mechanical basalt eruption model results showing the changes in crustal temperatures and densities due to evolving sill intrusions.  $\bar{z}_m$  is intrusion depth,  $\bar{\Phi}_m$  is magma flux,  $\bar{\rho}_{ob}$  is average density

of the overburden and  $\rho_m$  is magma density. The numbers 1 to 4 correspond to the stages of the system developments described in the text.



**Figure 4**

Time series of modeled global temperature variations and onsets of main-phase eruptions of Deccan Traps (abc) and CRBG (def). a,d sill intrusion depth and the timing of transition from mostly intrusion to major phase of extrusion, predicted by the thermo-mechanical model described in the Methods, given the indicated melt flux with time. CRBG case (d) has a lower peak flux of 10 cm/yr b,e, global averaged atmospheric CO<sub>2</sub> concentration with time predicted by the LOSCAR climate model. c,f global temperature change predicted by the LOSCAR model on top of climate data (Fig.1) and with the modeled timing of onsets of main-phase eruptions.

## Supplementary Files

This is a list of supplementary files associated with this preprint. Click to download.

- [Video1densityDeccan.mp4](#)
- [Video2pressuresDeccan.mp4](#)
- [Video3viscosityDeccan.mp4](#)

- [Video4FluxSillDepthTPBKDeccan.mp4](#)
- [Video5densityCRB.mp4](#)
- [Video6pressuresCRB.mp4](#)
- [Video7viscosityCRB.mp4](#)
- [Video8TandMBKPCRB.mp4](#)